



SIMULATION STUDIES TOWARDS AN
ORIENTATION CALIBRATION TECHNIQUE FOR
THE MULTI-PMT DIGITAL OPTICAL
MODULE IN FUTURE ICECUBE EXTENSIONS

MASTER THESIS

Master of Science, Westfälische Wilhelms-Universität Münster

Máster Interuniversitario en Física Nuclear, Universidad de Sevilla

By: Juan Bautista Bernal Florindo

Supervisor and first examiner: Prof. Dr. Alexander Kappes

Westfälische Wilhelms-Universität Münster

Second examiner: Prof. Dr. Francisco Javier García López

Universidad de Sevilla

Münster, December 2018

Contents

Contents	I
1 Preface	1
2 High energy neutrino astrophysics	3
2.1 Neutrinos in the Standard Model	3
2.2 Astrophysical neutrino sources	5
2.3 Detection of high-energy neutrinos with neutrino telescopes	7
3 The IceCube neutrino observatory	11
3.1 The IceCube and IceCube-Gen2 detector	11
3.2 Ice properties at South Pole	16
3.3 The multi-PMT digital optical module (mDOM)	19
3.4 Optical calibration devices	21
3.4.1 LEDs in optical modules	21
3.4.2 The Precision Optical CALibration Module (POCAM)	22
4 Orientation Calibration of mDOMs	24
4.1 General concept	24
4.2 Geant4 simulations	24
4.3 Angular acceptance simulations	27
4.4 Directional reconstruction of a point source	31
4.4.1 Initial approach	31
4.4.2 Likelihood reconstruction	44
5 Summary and outlook	64
6 Bibliography	67
List of Figures	71
List of Tables	78
Acknowledgments	81
Declaration	83

1 Preface

It is difficult to imagine that our body is at all times being crossed by a huge amount of one of the most elusive, imperceptible and difficult to detect particles in the universe, the neutrino. The neutrino was an idea that was born in the mind of the theoretical physicist Wolfgang Pauli in 1930 in order to explain the continuous energy spectrum of beta particles in the beta decay process. Thus arose the neutrino, a subatomic particle without electric charge, with angular momentum $1/2$ and with a very small mass that practically did not interact with anything. The neutrino could not be observed for many years after it was postulated but thanks to the work and perseverance of countless physicists and researchers its detection was achieved in 1956 by Clyde Cowan and Frederick Reines. We have managed to detect their presence even when they come from distant places of the universe. Significant advances have been made in the neutrino research field although much remains to be done.

Nowadays, the study of neutrinos has become one of the most prominent topics in current physics. Neutrino oscillations between the three different flavors and the estimation of their masses have captured the interest of numerous research groups, becoming one of the most prominent topics in 21st century physics.

The neutrino that is the most elusive particle of the universe is perhaps the one that carries the most accurate information about its structure and evolution. Neutrinos reach us practically without having suffered any interaction even though they may come from the most distant places. Cosmic rays like protons or other charged particles can be deflected by galactic magnetic fields, cosmic dust or radiation so we cannot know where the sources are. Neutrinos on the other hand are perfect messengers for cosmic objects since with their low interaction probability they can travel large distances without being altered. But this property of neutrinos makes them really hard to detect so to catch them we need huge detectors.

One of the most important current detectors in the study of neutrinos is IceCube which has been operating since 2011. To increase the detection rate of these neutrinos and to study their origin with greater precision, an IceCube Upgrade

is planned to increase the volume of the detector. In this upgrade new and more sophisticated modules with advantages with respect to those already installed in the current detector will be implemented. There will be also deployed better calibration devices. This new upgrade will also allow us to more efficiently search and locate the sources of neutrinos in the cosmos, which is undoubtedly one of the fundamental objectives of neutrino astronomy.

One of the new optical modules that will be implemented in the next IceCube Upgrade is the Multi-PMT digital optical module, or short mDOM. The mDOM includes 24 small photomultiplier tubes (PMTs) instead of a big one like current modules have.

The objective of this thesis will be the orientation calibration of these new mDOMs using a novel device called POCAM. There will be more calibration device like inclinometers and magnetic sensors. When modules are deployed in the ice, their orientation and exact position are unknown due to the refreezing process. This calibration is crucial when looking for cosmic sources of high energy neutrinos since it allows us to make more accurate event reconstructions.

2 High energy neutrino astrophysics

This chapter will provide a brief introduction to high-energy neutrinos, their place in the Standard Model, their sources and their interaction with matter thanks to which they can be detected with huge telescopes.

2.1 Neutrinos in the Standard Model

The Standard Model of particle physics describe the fundamental particles that constitute all the matter that we know. The standard model consists of 12 fermions and 5 bosons. The fermions are divided into 6 quarks and 6 leptons. Quarks are grouped into triples forming protons and neutrons and these in turn constitute the atomic nucleus of all known elements in the universe. Quarks have positive (up, charm, top) and negative (down, strange, bottom) charges. On the contrary, electrons, muons and taus that constitute the leptons have a negative charge although their masses are different, with the electron being the least heavy and the tau the most. In the lepton group we also find neutrinos, each lepton previously mentioned has its corresponding associated neutrino. Neutrinos are particles with zero electric charge and a very small mass. As we said before, the neutrinos that we find in nature are of three types: electron neutrino, muon neutrino and tau neutrino, also called neutrino flavors. The taste of neutrinos is not a property of these particles that remains immutable, these can change their flavor as they propagate in space through a medium or vacuum. This phenomenon is known as neutrino oscillation and is a subject of current research in physics. Although at first it was thought that neutrinos lacked mass, the phenomenon of the neutrino oscillation indicates that they must have a certain mass although this is very small in comparison with other particles of the standard model. The neutrino only interacts with matter through the weak interaction so its direct detection is practically impossible. Its detection is achieved indirectly via to secondary particles released in their interactions.

The anti-particles for leptons and quarks are also described in the Standard Model. These anti-particles have the same mass as their corresponding particle

but opposite quantum number. Lastly, we have the five gauge bosons corresponding to the four fundamental interactions and the Higgs field. We have the photon for the electromagnetic force, 8 gluons for the strong nuclear force, the bosons Z^0 and W^\pm for the weak nuclear force by which neutrinos interact with matter and finally the Higgs boson for the Higgs field. Photons and gluons lack mass but on the other hand the bosons Z^0 and W^\pm mediators of the weak nuclear force and the Higgs boson produced by the quantum excitation of the Higgs field are massive. All the elementary particles described are classified with their properties in the Figure 2.1.

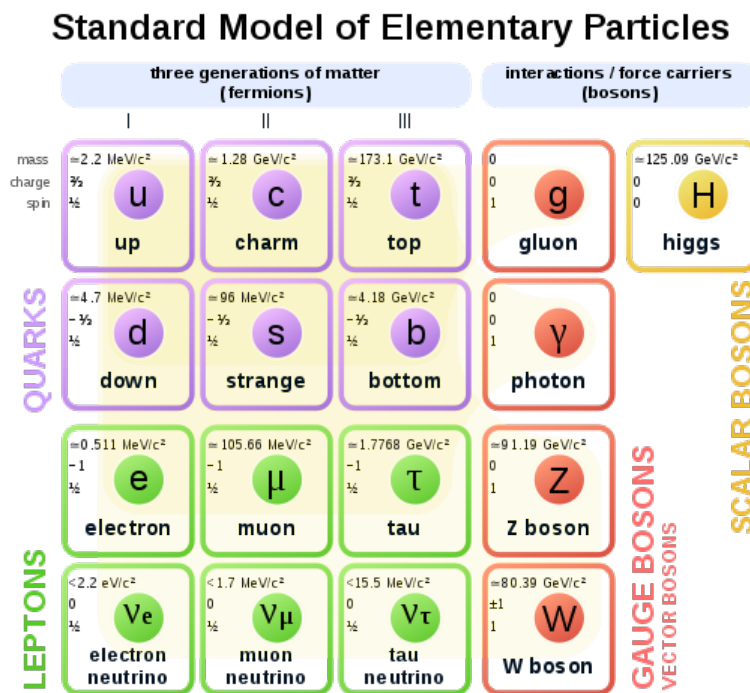


Figure 2.1: A depiction of the elementary particles in the standard model: The 12 fundamental fermions (purple and green) and 5 fundamental bosons (red). Fermions are constituted by quarks (purple) and leptons (green). Figure taken from [1]

Neutrinos only interact with other matter through weak interactions. For high energy neutrinos (10 GeV or higher) [2], the dominant interaction process is the deep inelastic scattering with nucleons. These reactions can be carried out via the neutral current (NC) or charged current (CC). These are mediated by the Z^0 and W^\pm bosons respectively. These reactions are shown in equation 2.1.

$$\nu_l + N \longrightarrow l + X \text{ (CC)} \qquad \nu_l + N \longrightarrow \nu_l + X \text{ (NC)} \qquad (2.1)$$

where ν_l represents a neutrino (or an antineutrino) with the lepton flavour l . N represents a proton or neutron, l represents the emitted lepton (or antilepton) and X represents the additional rest products of the interaction, which can be hadronic particles or a hadronic cascade.

2.2 Astrophysical neutrino sources

Neutrinos detected on Earth come from a wide variety of sources and processes, so they come with very different energies from μeV to EeV . Neutrinos can originate from sources as diverse as the Sun due to nucleosynthesis reactions that occur in it ($\text{keV} - 10 \text{ MeV}$) [3], from core-collapse supernovae via inverse beta decay ($\text{MeV} - \text{GeV}$) [4], natural radioactive decays (MeV) [5], the nuclear reactors that there are on Earth, atmospheric neutrinos generated by cosmic particles in the atmosphere, even primordial cosmological neutrinos, relics of the Big Bang ($\mu\text{eV} - \text{meV}$) [6] and from deep space. In Figure 2.2 we can observe the different neutrino fluxes for different energies stemming from terrestrial and cosmological sources.

Although the cosmic rays were discovered more than 100 years ago, it is still not clear the origin and process by which part of these particles are created reaching such high energy values. One of the most accepted theories is bottom-up mechanisms, which suggest that charged particles of low energy are accelerated gradually to the energies observed by extragalactic sources as active galaxies nuclei, SuperNova Remnants, pulsars, micro-quasars, Gamma Ray Bursts and starburst galaxies [8] [9].

The same processes that create high-energy cosmic rays may produce high-energy neutrinos as well, the sources are not known yet for sure but the possible sources are denoted cosmic particle accelerators [10]. High-energy neutrinos are the perfect messenger for the study and search of these sources of cosmic rays. Photons and cosmic rays formed by charged particles generated in these objects are not good candidates to track their sources since these particles can be deflected by magnetic fields in the case of charged particles or they can be absorbed or dis-

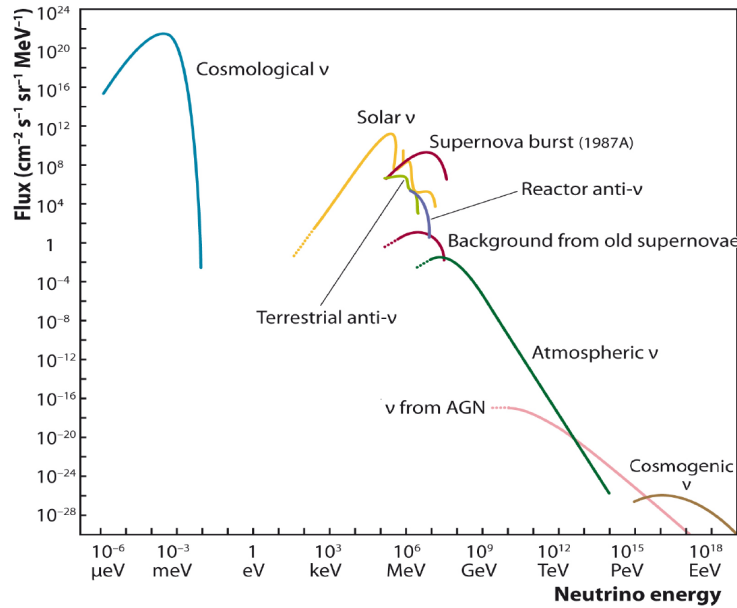


Figure 2.2: Neutrino fluxes detected on Earth from different sources. The region from tens of GeV to about 100 PeV, which feature much smaller fluxes than neutrinos of smaller energies, is addressed by Cherenkov light detectors. The highest energies are only accessible with huge volume detectors like IceCube. Figure taken from [7]

persed in the case of photons. When these particles reach us, they do not provide us with accurate information about the position of their sources in the cosmos and we cannot do a complete and good study about their sources and the reaction in which they were formed. Pierre Auger Observatory have observed clear anisotropies in cosmic rays flux at the highest energies (EeV) [11] [12]. Gammas have a cutoff at high energies and cosmic rays present uncertainties in the direction of their sources. This is where neutrinos come into play in high energy astrophysics with a role of great importance due to the properties they possess.

On 22 September 2017, IceCube detected the first possible source of high-energy neutrinos and cosmic rays. A high-energy neutrino event corresponding to a muon neutrino was coincident in direction and time with a gamma-ray flare from the blazar TXS 0506+056. It was found an excess of high-energy neutrino events with respect to atmospheric backgrounds at the position of the blazar between September 2014 and March 2015 with 3.5σ confidence level [13].

The small cross section of the neutrino also makes it a very difficult particle to detect. Although the effective interaction section of a neutrino with the matter

increases with the energy [9] so it would be easier to detect it, the flux of these energetic neutrinos is very low in comparison with other less energetic ones. So for its detection it is necessary detectors of large dimensions to have a good detection statistics.

2.3 Detection of high-energy neutrinos with neutrino telescopes

Detection in neutrino detectors is usually achieved indirectly through Cherenkov radiation induced by charged leptons. Large-volume detectors have been built in different places on Earth with transparent detection media like lakes, oceans or Antarctic ice and many of them are still functioning as ANTARES (Astronomy with a Neutrino Telescope and Abyss Environmental RESearch) [14] [15], Baikal Deep Underwater Neutrino Telescope (BDUNT) [16] and IceCube [17] or will be completed soon as KM3NeT [18].

ANTARES and BDUNT are located in the northern hemisphere and in both, water is used as a material medium to carry out the detection of neutrinos. ANTARES is located in the Mediterranean Sea, the detector consists of twelve columns anchored to the seabed, about 2500 meters deep, each containing 75 photomultipliers that collect the signals produced by Cherenkov effect [19]. The Baikal project located in Russia in lake Baikal has a similar structure.

IceCube on the contrary is located in the southern hemisphere and in this case the medium to carry out the detection of neutrinos is ice. IceCube consists of a cubic-kilometer of instrumented ice. Optical modules in the ice measure Cherenkov photons, produced by charged leptons travelling through the ice with speeds greater than the speed of light in the ice. These leptons were created in turn by neutrino interactions with ice.

The Cherenkov radiation is an electromagnetic radiation emitted when a charged particle passes through a dielectric medium at a speed greater than the phase velocity of light in that medium. When a charged particle travels through a dielectric medium, the electromagnetic field of the charged particle polarizes the local field in the surrounding medium. At low velocities the field falls back to

equilibrium shortly after the particle has passed through. However, when the speed of the particle is higher than the local speed of light in the ice, the response speed is lower than the travelling speed, so a shockwave of Cherenkov photons appears. The Cherenkov radiation photons are emitted in the form of a cone in a direction forming an angle θ_C with the path of the charge particle. The angle is given by:

$$\cos \theta_C = \frac{1}{n\beta}. \quad (2.2)$$

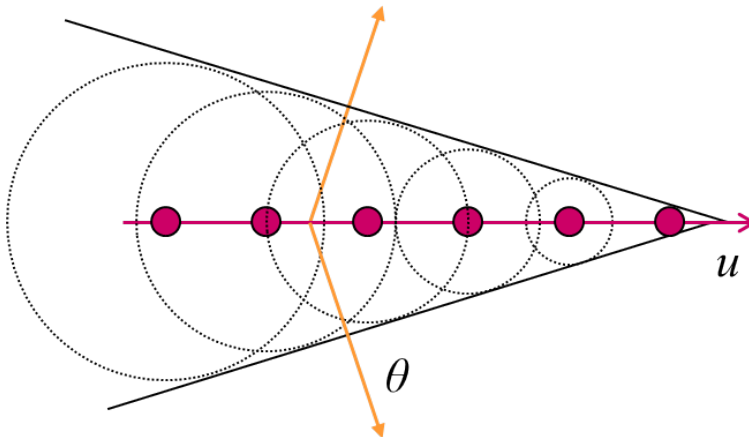


Figure 2.3: Cherenkov radiation cone along the trajectory of a fast moving charged particle with speed u that moves faster than light in that medium. θ is the angle between the direction of movement of the charged particle and the Cherenkov photons.

Where n is the refractive index of the medium, $\beta = v/c$ where c is the speed of light in vacuum and v is the charged particle's speed in that medium. The original charged particle direction can be reconstructed thanks to the Cherenkov light considering that we know the relative movement between the Cherenkov photons and the path of the charged particle. The Cherenkov angle for ultra-relativistic particles ($\beta \approx 1$) travelling through ice ($n = 1.3$) is approximately $\theta_C = 42^\circ$.

The amount of energy radiated per unit of length is given by the Frank-Tamm formula [20] as:

$$\frac{dE}{dx} = \frac{e^2}{c^2} \int \left(1 - \frac{1}{\beta^2 n^2(\omega)} \right). \quad (2.3)$$

Where ω is the angular frequency and e is the charge quantum. The amount of Cherenkov photons N_γ radiated per unit length x with a wavelength λ emitted by

a particle is described by an alternative expression of the Frank-Tamm formula [20]:

$$\frac{d^2 N_\gamma}{dx d\lambda} = \frac{2\pi\alpha}{\lambda^2} \cdot \left(1 - \frac{1}{\beta^2 n^2(\lambda)}\right). \quad (2.4)$$

Here, $\alpha \approx 1/137$ is the fine-structure constant.

The Cherenkov light is collected by photomultipliers placed in the optical modules. These devices convert photons into measurable electrical signals and are extremely sensitive. With them we are able to even detect single photons. The operation of the multiplier is described by numerous parameters and properties of the materials that form it. Among them, the quantum efficiency, the dark rate, the gain, the transit time and the transit time spread (TTS). The incident light reaches the photocathode, a photosensitive material with a high probability of photoelectric effect. Here comes into play the quantum efficiency since not all photons that arrive at the photocathode pull out photoelectrons. The quantum efficiency is defined as the number of photoelectrons emitted by the photocathode divided by the number of incident photons. For an ideal photocathode the quantum efficiency would be 100% but practically photocathodes show maximum quantum efficiencies of 20-30%. The quantum efficiency of the PMT depends on the wavelength of the incident light. As the number of photoelectrons that are released is very small, the number of electrons is amplified by a series of dynodes connected to increasing positive potentials. The electrons are attracted by the first dynode, collide with it and release more electrons (secondary electrons), which in turn are attracted by the next dynode that is at a higher potential and so on until reaching the anode which collects all the electric current produced. This process in which the number of electrons collected is increased is described by the gain of the detector. The transit time is the time between the photon reaching the photocathode and the whole charge is collected in the anode. This time is not constant, and therefore the transit time spread is defined as the standard deviation of the transit time distribution. The transit time spread determines the time resolution of the photomultiplier. It may also happen that electrons are emitted when no photons hit the photocathode, this is known as the dark rate of the PMT. The PMT arranged in the modules have both an own dark rate and a dark rate induced by radioactive decays in the crystal and gel that form the

module in IceCube.

We can see a scheme of a PMT and how the photons are detected in the Figure 2.4. Photomultipliers perform this charge amplification in a very linear manner so the electric charge collected in the anode provides us information about the amount of the incident photons. Typical tubes, when illuminated by a very short duration light pulse, will produce an electron pulse with a time width of a few nanoseconds after a delay time of 20-50 ns [21]. More information on these topics can be found in [21].

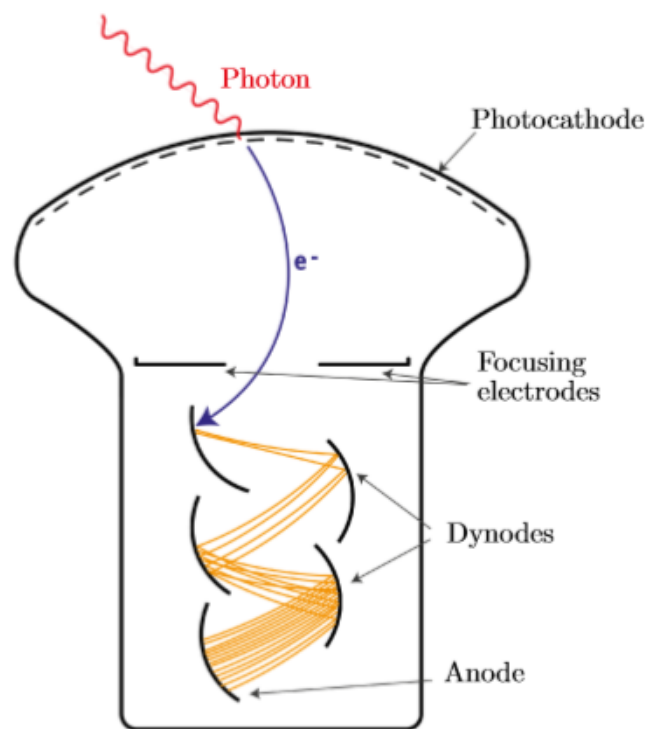


Figure 2.4: Schematic of a photomultiplier tube and its main constituents. The green sinusoidal line represents a photon that emits a photoelectron (blue line) at the photocathode realising secondary electrons from the dynodes. The total charge is collected at the anode. Figure taken from [22]

3 The IceCube neutrino observatory

In this chapter the South Pole neutrino observatory will be described. The current modules that form IceCube and a new module that will be implemented in the next updates that will be carried out on it. The optical calibration devices will be described as well.

3.1 The IceCube and IceCube-Gen2 detector

The largest neutrino detector that currently exists is the IceCube project. The IceCube Neutrino Observatory is located in Antarctica, the medium to carry out the detection of neutrinos is ice. At a depth of one kilometer, the pressure is so great that there are no air bubbles present in the ice, the medium is extremely transparent and there are very few contaminants making it an ideal medium for the detection of neutrinos. A primary goal of IceCube is to clarify the production mechanisms of high energy cosmic rays by detecting high energy neutrinos from astrophysical sources. The IceCube project occupies a volume of one cubic kilometer and consists of 86 strings located at a depth between 1450 and 2450 m each holding 60 digital optical modules (DOMs) in intervals of 17 meters. These 5160 DOMs are made up of a ~ 10 inch PMT facing down with a timing resolution of less than 5 ns and a quantum efficiency of 25% for a wavelength of 470 nm [23]. The entire module is covered by a spherical 13-inch glass pressure vessel making them be able to survive extreme conditions of pressures and temperatures. This modules are capable of withstanding temperatures down to -70° [24] and pressures of 70 MPa [25]. The module is also shielded by a mu metal grid against magnetic fields [26]. The horizontal distance between strings is 125 meters. The bulk of IceCube is sensitive to neutrinos with energies above 100 GeV. Located at the centre of the detector we find DeepCore which is a more dense instrumented sub-detector formed by eight strings separated by 72 meters whose goal is to detect lower energetic neutrinos featuring energies as low as 10 GeV. IceCube contains in total about 5160 photomultipliers all of them are pointing down to eliminate as much as possible the muons produced by the cosmic rays in the atmosphere using the planet itself as a shield. IceCube Neutrino Observatory

and their current modules are shown in Figure 3.1.

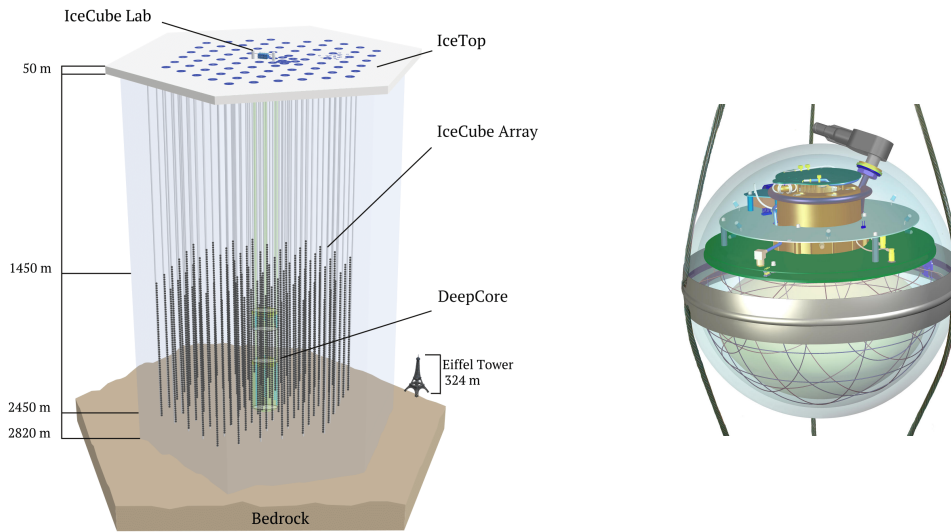


Figure 3.1: **Left:** Image of the IceCube Observatory at the South Pole with all their components: the high-energy array, the low-energy extension DeepCore and IceTop on the surface. **Right:** Image of The IceCube DOM. It consists of a glass pressure sphere with a 10 inch PMT facing down in the lower half and readout electronics. Figures taken from [27].

The interactions described in the previous chapter cause typical signatures in the detector depending on the flavor of the neutrino that produced the reaction. There are two basic topologies: tracks from muon neutrinos and cascades from electron neutrinos, double bangs from tauon neutrinos.

The Tracks are signals left by muons that travel long distances (\sim km) in the detector product of the reaction of a muon neutrino in the ice. With these signals we can make a precise directional reconstruction with accurate angular resolution, that is, they are good particles for the research of point sources since the direction that these muons have does not deviate much from the one that the neutrino carried. IceCube's angular resolution is accurate for long tracks but the reconstruction of the neutrino energy is difficult to achieve due to this events are partially contained in the detector and also due to the background of atmospheric muon neutrinos [23].

The Showers are spherical marks in which at its center a greater number of photons are produced, these do not cross long distances in the detector since the energy is deposited in a small volume of it (10 meter-long). With this type of

signals, a good estimation of the neutrino energy can be made, although on the contrary, they do not offer precise information on the direction of the neutrino.

Double Bang is the signal registered in the detector caused by a high energy tau. At PeV energies the tauon travels some hundreds of meters and it decays producing a second cascade.

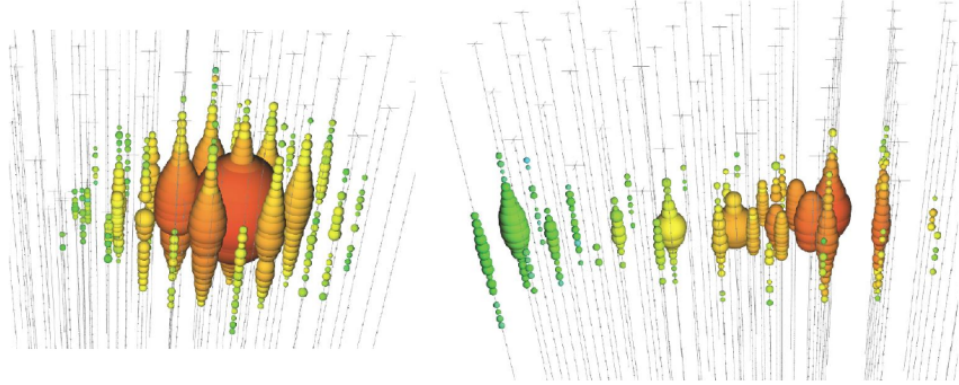


Figure 3.2: Light deposition signatures of a shower (**left**) and a track (**right**). Modules are drawn as dots, the color gives information about the arrival time of photons, going from red (early) to blue (later) and the size of the dots about the amount of detected light. Figure taken from [27]

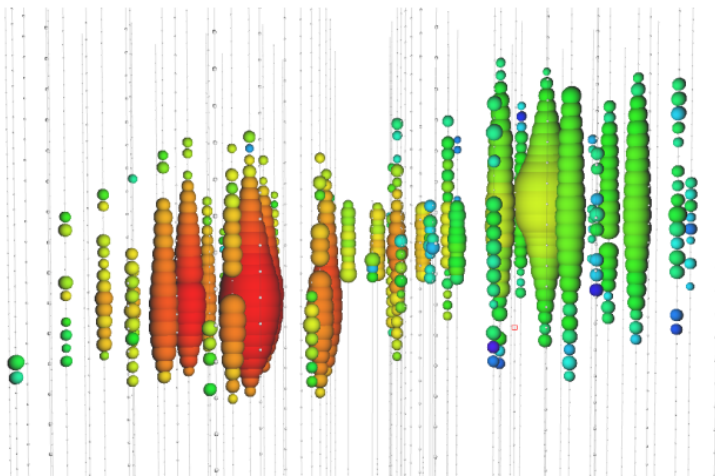


Figure 3.3: Expected double bang event signature from a high energetic τ neutrino. This event have been simulated even though there are already some double bang candidates. Figure taken from [27]

With the aim of increasing the detection rate of these high-energy neutrinos and thus being able to find the sources from which they come, an IceCube extension called IceCube-Gen2 is being planned. It will be build around the current IceCube

detector. This extension will increase the in-ice instrumented volume by a factor of up to ten. There will be implemented around 120 new strings, each one with 125 new modules. These new modules are more sophisticated and have some advantages over their predecessors. The new high-energy array will contain about 15000 new optical sensors [28].

Since the optical properties of the glacial ice are better known now we also know the absorption length of the ice for Cherenkov light is larger than initially assumed. This enables the instrumentation of considerably larger volumes with lower string densities than in IceCube. The string separation that is being considered lies between 240 and 300 meters [28]. A possible configuration of the IceCube-Gen2 telescope is shown in Figure 3.4.

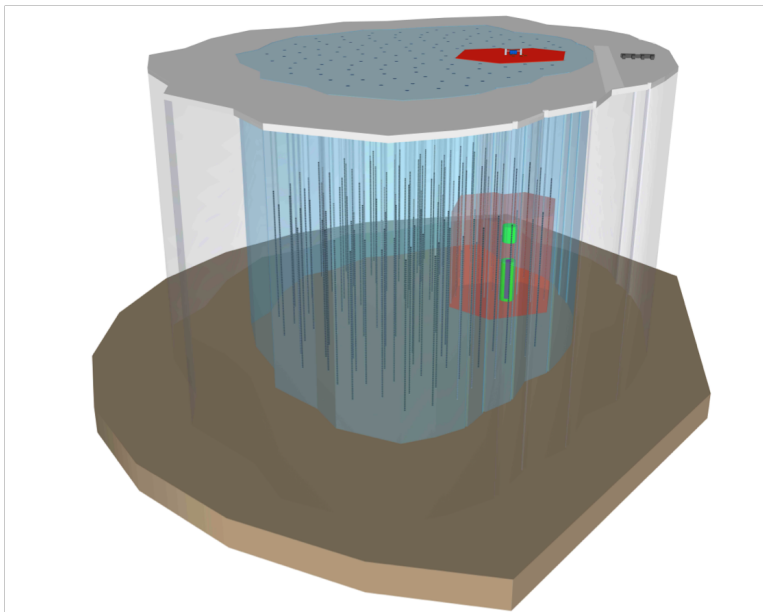


Figure 3.4: A possible IceCube-Gen2 configuration. IceCube, in red, and the infill subdetector DeepCore, in green, show the current configuration. The blue volume shows the full instrumented next-generation detector. Figure taken from [27]

Currently, the first step in a long process developing IceCube-Gen2 has already been approved. This first update named IceCube Upgrade will take place during 2021, which will implement seven new chains at the bottom of the detector array.

With this new update we will have a higher performance of IceCube at low energies, the detection rate of atmospheric neutrinos will increase by a factor of ten, likewise the pointing resolution of the astrophysical neutrinos will be

improved. IceCube due to the new deployment of the arrays in the Upgrade will have the best measurements of the world in neutrino oscillations.

The new strings will increase the light collection by reducing the separation between the IceCube ropes from 125 to 75 meters and the distance between the light sensors along a string of 17 to 2.4 meters [29]. There will be several new modules that will be deployed in this new IceCube update. It has not yet been decided which of the new modules will be used in IceCube-Gen2 but this first new update will undoubtedly be a good opportunity to test them. The seven new chains will be deployed with vertical and horizontal spacing that is three times smaller than DeepCore and will also include advanced calibration devices. A possible configuration of the IceCube Upgrade is shown in Figure 3.5.

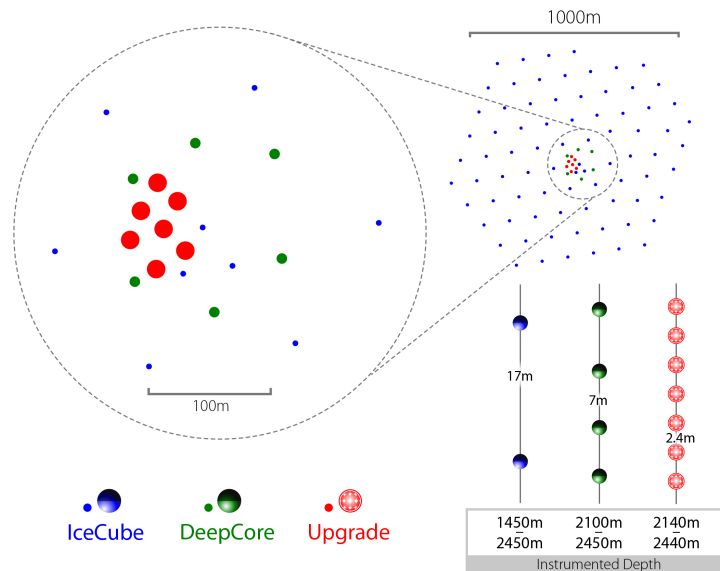


Figure 3.5: The modules of the IceCube Upgrade will be deployed with vertical and horizontal spacings three times smaller than DeepCore. Figure taken from [27].

The new calibration devices will allow better knowledge about ice properties and the position of the modules which leads to better reconstruction of cascaded events and better identify tau neutrinos. Cascade signatures have a resolution worse than the tracks although they constitute more than 75% of the processes detected in IceCube. Cascades allow reconstructing the direction of the incoming neutrino with a typical angular resolution of 5-10 degrees, while tracks point to the neutrino's origin to within less than 1 degree [23]. The refined calibration of

the existing sensors will also enable a reanalysis of more than ten years of archival data.

At the moment, IceCube has provided us with very good measurements in neutrinos and multimessenger astronomy, it has been able to detect very high energy astrophysical neutrinos, the first probable source of neutrinos and cosmic rays has been identified, which is an important first step for the complete mapping of all of them in space. It has also provided us with information regarding the oscillations of neutrinos. IceCube telescope will allow us to explore the most violent astrophysical processes associated with the origin of the universe and it also might open the possibility of totally new discoveries.

3.2 Ice properties at South Pole

One of the main characteristics that sets apart the glacial ice from other mediums used in Cherenkov detectors, such as marine water or fresh water, is that in the glacial ice there is no bio-luminescence and the rate of radioactive decays is very low. Low temperatures also decreases the background noise of the intrinsic dark rate of the PMTs even though glass background increases [22].

When using ice as the medium for the Cherenkov radiation, the optical properties of ice must be known in detail in order to accurately interpret the measurements. These are the optical absorption and scattering of the radiated photons. Compared to water, deep ice generally has longer absorption lengths but shorter scattering lengths. The optical properties of ice strongly depend on impurities, such as dust, introduced into the ice when it was first deposited by snowfall. Therefore, the ice also presents a series of characteristics that are not advantageous with respect to water as depth-dependent variations of the absorption and of scattering lengths due to the different amount of dust. Due to the size of the dust particles Mie scattering prevails over Rayleigh scattering for photons propagating through the South Pole ice [30]. In addition, a slight azimuthal dependence of the light propagation properties was found which can be attributed to an apparently smaller amount of scattering in one direction [31].

In IceCube, the LED flashers offer a way to study the ice. This has resulted in

more and more refined ice models. Both the absorption length and the scattering length of the light have been measured for different wavelengths by measuring the arrival time distributions of the photons from LEDs in a DOM measured by other DOMs [31]. The sum of the statistical and systematic uncertainties in the measured values of the effective scattering and absorption coefficients inside the instrumented volume of the IceCube detector was estimated to be around 10% [24].

The expressions of scattering and absorption lengths have been calculated in function of depth-dependent parameters $b_e(400)$ and $a_{dust}(400)$ related to scattering and absorption at a wavelength of 400 nm, by the depth-dependent relative temperature $\delta\tau$, and by six global parameters in [30] and [24] as a function of the photons wavelength and the depth. The geometrical scattering coefficient b determines the average distance between successive scatters as $1/b$. Although sometimes it is more convenient to use the effective scattering coefficient b_e :

$$b_e = b \cdot (1 - \langle \cos(\theta) \rangle). \quad (3.1)$$

Where θ is the deflection angle at each scattering. The absorption coefficient a determines the average distance traveled by a photon before it is absorbed as $1/a$.

Next we present the wavelength dependence expressions of the scattering and absorption coefficients for wavelength λ in nm. The power law dependence was verified by AMANDA studies using light sources with different frequencies [24]. The effective scattering coefficient, with the global fit parameter α , is:

$$b_e(\lambda) = b_e(400) \cdot \left(\frac{\lambda}{400} \right)^{-\alpha} \quad (3.2)$$

The parameters α was calculated in [24] being $\alpha = 0.90 \pm 0.03$.

The total absorption coefficient is the sum of two components, one due to dust and the other a temperature dependant component for pure ice. It is given by [30] and [24] as:

$$a(\lambda) = a_{dust}(\lambda) + A \cdot e^{-B/\lambda} \cdot (1 + 0.01 \cdot \delta\tau) \quad (3.3)$$

with

$$a_{dust}(\lambda) = a_{dust}(400) \cdot \left(\frac{\lambda}{400} \right)^{-\kappa} \quad (3.4)$$

The remaining parameters have been calculated in [30] to $A = (6954 \pm 973) \text{ m}^{-1}$, $B = (6618 \pm 71) \text{ nm}$ and $\kappa = 1.08 \pm 0.01$. The $\delta\tau$ is a temperature parameter which represents the temperature difference relative to the depth of 1730 m:

$$\delta\tau(d) = T(d) - T(1730\text{m}) \quad (3.5)$$

and the temperature $T(\text{K})$ is parameterized in [24] as:

$$T = 221.5 - 0.00045319 \cdot d + 5.822 \cdot 10^{-6} \cdot d^2 \quad (3.6)$$

The figure 3.6 shows the absorption and dispersion distances currently used in IceCube as a function of depth and wavelength. These curves are based on theoretical models adjusted to the measurements carried out by AMANDA and IceCube. The effect of air bubbles and dust peaks is visible. The probability for photons to be absorbed is higher for larger wavelengths, meanwhile the probability for photons to suffer Mie scattering is higher for smaller wavelengths.

The majority of calculations in this work will be done in the clean part of the ice, at the depth of 2278.2 meters where $1/a(400) = 227.2 \text{ m}$ and $1/b_e(400) = 76.8 \text{ m}$.

In addition, by introducing the detector modules into the ice where the ice had been melted with a hot water drill, anisotropies were introduced in the refreezing process of the perforated holes due to contamination. The new optical properties of the drill holes in IceCube must be measured again. Although the photon only travels a small part of its path through the drill hole, the optical properties of these drill holes should be better understood since they are currently one of the largest uncertainties to neutrino oscillation measurements in IceCube [32]. Some of the experimental approach to determine in situ the scattering properties of the refrozen drill holes consist in using the LEDs already installed in the DOMs and

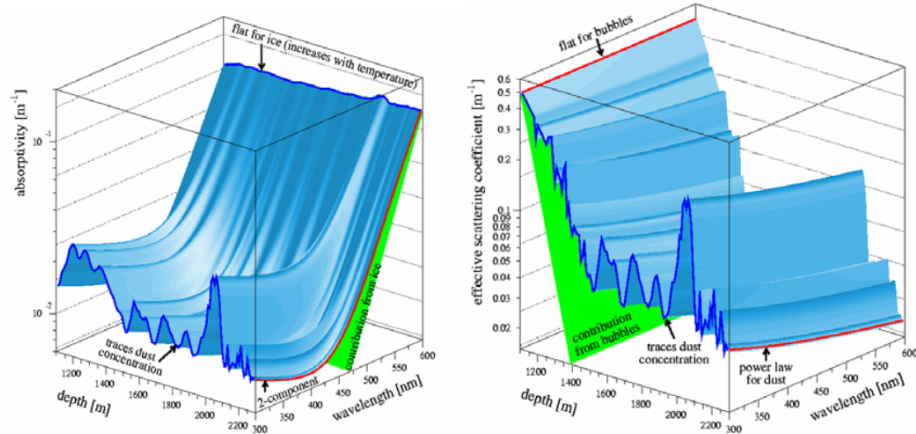


Figure 3.6: Deep ice optical properties. Absorption length (left) and scattering length (right) of light in the South Pole ice as a function of depth, from 1100 m to 2300 m and wavelength, from 300 to 600 nm. Figure taken from [30].

detect the light emitted for the LED by the photomultiplier of the same DOM [33].

3.3 The multi-PMT digital optical module (mDOM)

One of the new modules that will be deployed in the IceCube-Upgrade is the multi-PMT digital optical module (mDOM). Due to their novel properties, the new digital optical modules for IceCube-Gen2 will improve the measurement characteristics. The design of the module is based on the optical modules of KM3NeT. Unlike the current DOMs in IceCube which feature a 10-inch PMT pointing down, the mDOM is constituted by 24 PMTs of 3 inches facing multiple directions. The mDOMs can detect photons from any direction thanks to the distribution of their PMT unlike the DOMs that can only detect photons from the region of the space to which they point. In addition, the PMTs are surrounded by reflectors that provide stronger directionality. All components of the mDOM are protected by a glass pressure vessel so that they can withstand the extreme temperature and pressure conditions to which they are subjected. For the mDOMs the diameter of the spherical pressure vessel is 14 inch. The mDOM has a layer of optical gel between the vessel glass and the internal components of the module whose aim

is to prevent light reflections due to the different refractive indices of glass and providing structural stability. The structure of the mDOM and its components are shown in Figure 3.7. This new modules present several attractive advantages compared to the current single-PMT DOM already installed, like:

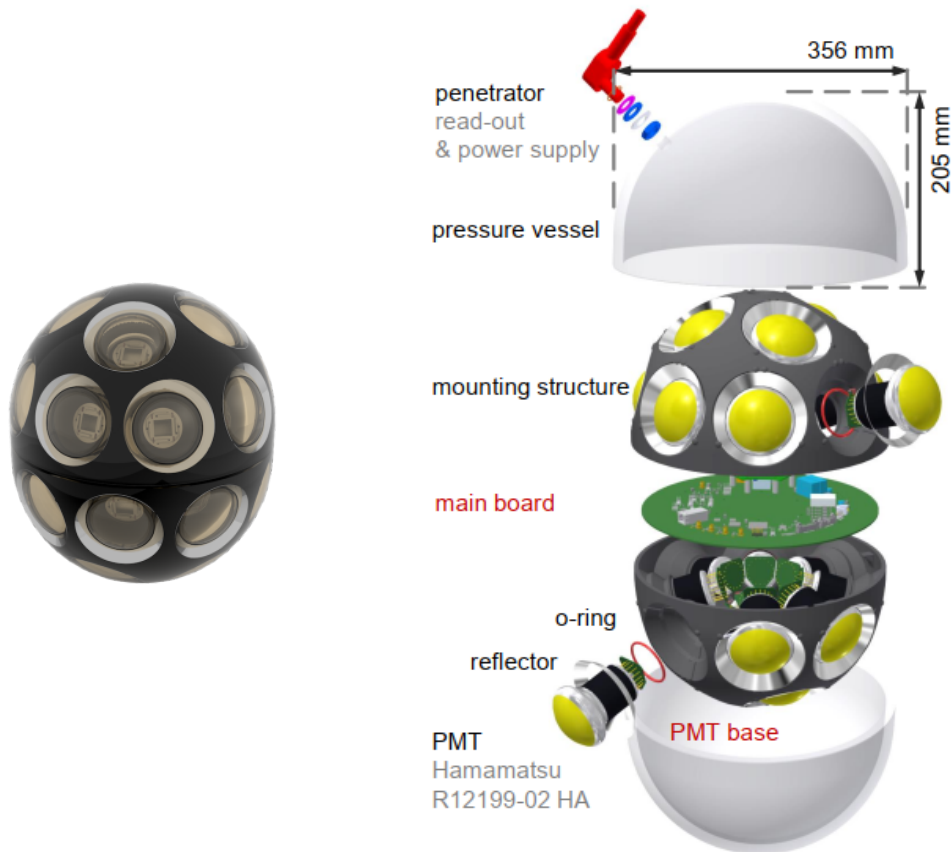


Figure 3.7: **Left:** Rendered image of the mDOM with 24 PMTs inside the pressure vessel. **Right:** Exploded view of the mDOM, with its different components. Courtesy of the IceCube Collaboration.

- Larger photocathode area: 24 3-inch PMTs provide a larger effective area than one 10-inch PMT.
- Superior photon counting: By having a greater number of PMTs covering the same region of the space we will have a better count of photons since these will be detected by different PMTs. The number of photons and the time of arrival of each of them can be easier reconstructed.
- Improved angular acceptance: The mDOMs present a near homogeneous 4π angular acceptance due to the distribution of the PMTs on it covering all

directions. On the contrary, the DOMs have practically no sensitivity (only contribution due to scattering in ice) in the opposite direction towards which they are pointing.

- **Intrinsic directional sensitivity:** The orientation of the PMTs in the mDOM together with the angular acceptance of each PMT gives us more precise information about the direction that the photons were detected, thus making possible an improved reconstruction of the events.
- **Local coincidences:** With several PMTs in the same module we can detect coincidences between these PMTs of the same module. This allows us to eliminate the uncorrelated single-hit noise and also PMT self-calibration. Local coincidences are also useful for better reconstruction of low-energetic neutrinos as for example neutrinos coming from supernova explosions.

3.4 Optical calibration devices

In this session a brief summary of the IceCube optical calibration devices is provided. These are the LEDs, already implemented in the current IceCube modules (DOMs) and the future POCAMs that will be installed as a complementary calibration device in the future IceCube Upgrade in which the new modules (mDOMs) will also be included.

3.4.1 LEDs in optical modules

The current modules of the detector are provided with these calibration devices. The LED flasher board in IceCube has been of great importance in measuring ice properties, timing, DOM sensitivity, location and orientation of the DOMs after deployment. It consists of 12 LEDs of known brightness placed in pairs around the flasher board. The beams are directed radially outward in six different azimuthal angles with an angular separation of 60° . Of each pair, one is pointed horizontally, and the other upwards at an angle of 40° . The total output from the LED ranges from approximately 10^6 to 10^{10} photons. The angular spread of each beam is modelled with a gaussian profile with $\sigma = 10^\circ$ [24].

With the Upgrade that will be installed in IceCube not only the new modules described above will be implemented with their respective LEDs but also a new and improved device for the calibration of these modules. This is the POCAM and will be described in the following section.

3.4.2 The Precision Optical CALibration Module (POCAM)

In the current detector, LEDs have provided a level of precision required for the present operation but it lacks an in-situ monitoring of the emitted light. LED-to-LED variations, individual DOM sensitivity variations and the optical properties of the refrozen hole ice are the main factors limiting the precision currently obtained in IceCube.

To improve the performance of the detector it is necessary to increase the precision by better understanding the optical properties of the deep ice. Here comes into play the Precision Optical CALibration Module (POCAM) which is an isotropic, multi-wavelength, and pulsed light source dedicated to in-situ self-calibration of the IceCube-Gen2 neutrino detector. The main goal of the POCAM is to reduce the systematic uncertainty coming from a partial understanding of the optical properties of the ice and the efficiency and angular acceptance of the IceCube digital optical modules from 10% to a level of few %. This new calibration device will be a complementary calibration system that will work together with the one presently installed in IceCube. To be able to determine in situ the relative optical efficiency and hole ice properties of the nearby DOMs there will be placed two POCAM modules on each array. With them will be re-evaluated the within the Gen2-Upgrade volume and the rest of the detector. Preliminary results indicate that output isotropy is achieved beginning with distances larger than 20 m from the module. The design of POCAM is based on the principle of an inverted integrating sphere. An appropriately placed matrix of LEDs in combination with a diffusing layer on the inside of the sphere results in a nearly homogeneous light emission. The output of the LEDs is monitored in-situ to high precision by photosensors, ensuring control over the light output.

Its design is shown in Fig 3.8. The POCAM is formed by two glass hemispheres connected by a cylindrical pressure and temperature-resistant titanium housing. The light source will be a matrix of 4 fast-switched LEDs driven by a Kapustinsky-

style circuit covering a wavelength range between 370 and 500 nm with two different light pulse configurations (5-10 ns, 15-25 ns) to obtain pulses of approximately 10 ns and $10^8 - 10^{10}$ photons per pulse [34]. These pulses are diffused by two spheres installed in each hemisphere made from a highly reflective material. These diffusing spheres convert the strongly anisotropic light from the LEDs to isotropic and homogeneous light for the illumination of the ice.



Figure 3.8: POCAM design: It is composed of four sub-systems: the pressure housing, the digital and the analog circuit boards, and the light diffuser elements.

Two photosensors are installed in each hemisphere to monitor the emitted pulse. The pressure housing is a 15 mm thick titanium cylinder, the two open sides of which are each closed by a flange and a glass hemisphere attached to it. The glass hemispheres made of BK7 glass have a thickness of 7 mm and a diameter of 4.5 inches. The entire housing is able to withstand hard pressure conditions and it can resist a pressure of at least 1500 bar [35].

The POCAM isotropic light emission pattern has clear advantages over the LEDs currently used. This isotropic light pattern allows the direct measurement of the individual relative efficiencies of the DOM, which despite being well restrained on average, the individual values deviate up to 10 % due to fluctuations in the quantum efficiency of the PMTs and the effects of local ice. The calibrated light output of the POCAM allows us to imitate the luminous signature of the high-energy cascades. This allows us to test the reconstructed cascade energy scale to the uncertainty in which the total photon output of POCAM is known.

4 Orientation Calibration of mDOMs

4.1 General concept

As already mentioned, one of the advantages of the mDOM with respect to the DOMs is its intrinsic directional sensitivity. The new POCAM calibration module that will be implemented in IceCube will allow us to determine in-situ the orientation of each mDOM after the refreezing process.

In reality when the new modules are deployed in the next IceCube upgrade, there will be an uncertainty in the orientation and real position of the mDOM in the ice. In this thesis, to carry out the orientation calibration for the multi-PMT digital optical module, Geant4 simulations were used. In these simulations, unlike in the real case, mDOM orientation and position is known at all times. What is going to be estimated is the angular position of the POCAM simulated as an isotropic point light source. The uncertainty of the reconstruction of the angular position of the light source is the equivalent of the uncertainty of the mDOM orientation if the exact position of the POCAM is known.

4.2 Geant4 simulations

These Geant4 simulations describe the interactions of the photons traveling through the ice, where the mDOM and the different sources used for this calibration technique are placed. In this thesis, a modified version of the simulation initially written in the framework of two PhD thesis [36] [37] for the simulation of the mDOM response is used.

These simulations are based on Geant4 which is a C++ software toolkit developed at CERN for the simulation of the passage of particles through matter using Monte Carlo method. Its development, maintenance and user support are taken care by the international Geant4 Collaboration [38]. Geant4 is being used in a large number of research fields, such as high energy physics, nuclear experiments, medical, accelerator and space applications.

The geometry of the module and the properties of the materials used are included in the simulation, as well as the physical processes and interactions of the particles with the materials. In the Geant4 base code, a large set of physical models is included to calculate the interactions between particles and matter in a very wide range of energies, all these processes have been validated experimentally [39].

In Geant4 one can define primitive volumes by means of geometrical figures and by using Boolean operations. To these volumes a specific material is assigned with its corresponding physical properties delimiting and defining the possible interactions with particles. The most important properties for the simulations will be the absorption length and the scattering length of the medium of interest, the ice of the South Pole. The simulations begin with the creation of photons and their initial conditions: energy, position and direction. These propagate through the volume of simulated ice and can be absorbed or scatter. The simulation of a single primary particle like the photon is called an event. A “track” object contains the trajectory and additional information of individual particles. A track is made up of steps, one for each interaction of the particle.

The simulation includes the external parts of the module (with their corresponding properties): the pressure glass vessel, the PMTs, the reflector cones and the optical gel. The PMT is modeled as a solid glass containing the photocathode. These components are Vitrovex glass for the pressure vessel, QSI-QGel 900 optical gel and Alemco V95 reflector cones. In previous studies about optimization of the reflector angle it was obtained that for vertical arriving photons the highest effective area corresponds to a cone angle of 51° [36], thus this angle was used in this work. The holding structure is simulated as a totally absorbing massive object. In the simulation, when a photon reaches the surface of the photocathode, it is removed and saved as a hit. The quantum efficiency (QE) of the photomultipliers was not considered in the simulations, i.e. each photon that hits the photocathode of the PMT is registered as a count. In Tab. 4.1, the “physicslist” used in Geant4 for the simulations of this work is described.

The world is defined as a sphere in the simulation. The mDOM is placed in the center of the sphere and its radius is equal to the distance at which the point source is placed. The wavelength of the photons used in the simulations is 470 nm. The calibration device POCAM is simulated with 10^9 photon events at the world boundary with isotropic direction. Many of the trajectories of the

Table 4.1: Description of the different physical processes and their corresponding class in Geant4 for the particle of interest in the simulations, the photon.

Particle	Process	Geant4 Class
Photon	Absorption	G4OpAbsorption
	Optical processes at medium interfaces	G4OpBoundaryProcess
	Mie scattering	G4OpMieHG

photons that are not directed towards the module are not calculated since they leave the world defined in the simulation. These simulations were performed for different angular positions of the source, distances and ice properties. In addition, “mDOM scans” were performed in which $10^6 - 10^7$ mono-energetic photons were simulated towards the mDOM from a plane disc, the direction of the photons is perpendicular to the disc surface and the density profile across the plane is constant. The distance between mDOM center and the plane disc is 30 cm. The absorption and scattering were deactivated for these scans simulations. These scans will be the model to carry out the angular reconstruction of the point source. An example of these simulations with only a few events are shown in Figure 4.1.

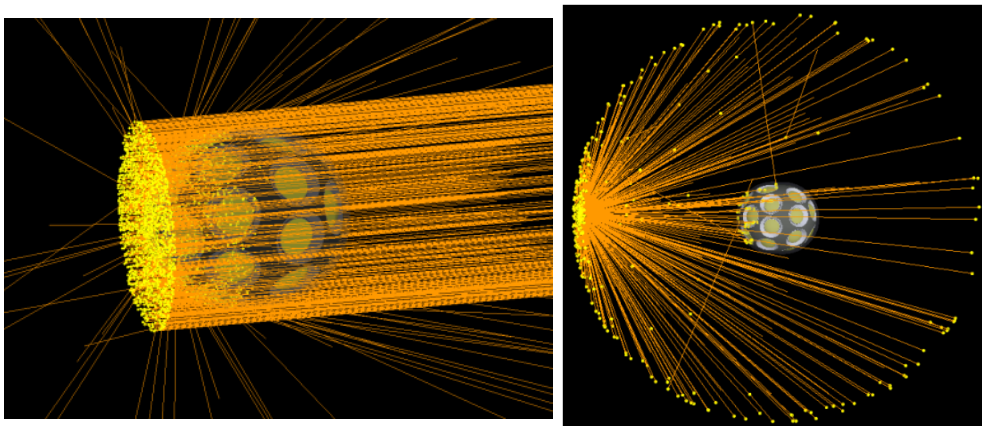


Figure 4.1: **Left:** Scan simulation for a certain angular position made on the mDOM in which photons are simulated from the normal direction to a plane disc. **Right:** POCAM simulated as an isotropic point source.

4.3 Angular acceptance simulations

The angular scan of the module allow us to calculate the angular acceptance of the module, in terms of an effective detector area as a function of the angle of incidence of a plane wavefront. The incidence direction of the light coming from a plane wavefront or a punctual source is defined in terms of θ and φ . As depicted in Figure 4.2 for two different plane wavefront. In the configuration of the mDOM, the hemispheres are not completely symmetrical, there is a rotation of 22.5° between them as can be observed in the Figure 4.2.

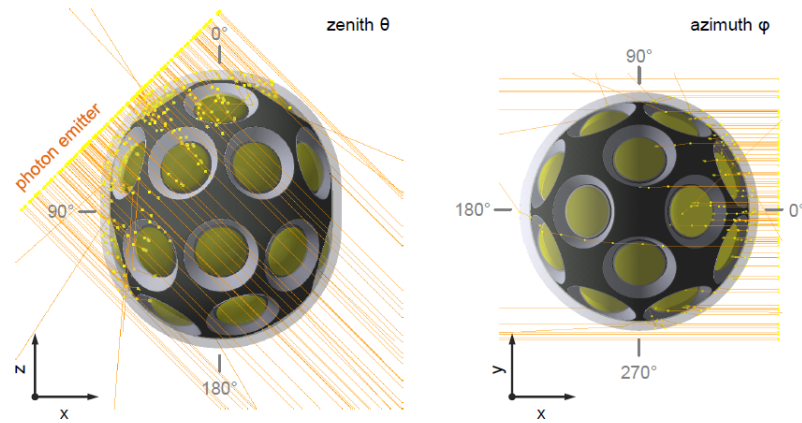


Figure 4.2: mDOM illumination from $(\theta = 45^\circ, \varphi = 0^\circ)$ (left) and $(\theta = 90^\circ, \varphi = 0^\circ)$ (right). Figure taken from [36].

The effective area A_{eff} of each PMT is calculated by means of the following expression:

$$A_{\text{eff}}(\theta, \varphi) = \frac{N_{\text{det}}(\theta, \varphi)}{N_{\text{emit}}} \cdot A_{\text{rad}}, \quad (4.1)$$

where $N_{\text{det}}(\theta, \varphi)$ is the number of detected photons for a plane wave from θ and φ , N_{emit} is the number of emitted photons and A_{rad} is the area of the radiating disc plane. Initially, the study was initiated with the scans made in [36]. In these investigations, 10^6 photons of 390 nm were simulated per angle position towards the mDOM with a plane disc of 24 cm radius. This wavelength was originally selected since it corresponds to the maximum quantum efficiency of the PMTs. A

second scan on the mDOM was also carried out with a total number of photons emitted by the plane disc of 10^7 and a wavelength of 470 nm. For the first scans made on the mDOM, photons were simulated from plane discs varying their angular positions degree by degree in both θ and φ collecting a total of 65160 angle pairs. In the second scan the amount of angular positions was increased and it consists of a total of 786432 angle pairs. More details about this scan can be found in section 4.4.2.

The angular effective area can be interpreted as the field of view of the mDOM or a particular PMT. This is depicted for single PMTs in Figure 4.3. Taking into account all PMTs that make up the module we have a near homogeneous 4π angular effective area. The angular effective area of the module is shown in Figure 4.3, 4.4 and 4.40.

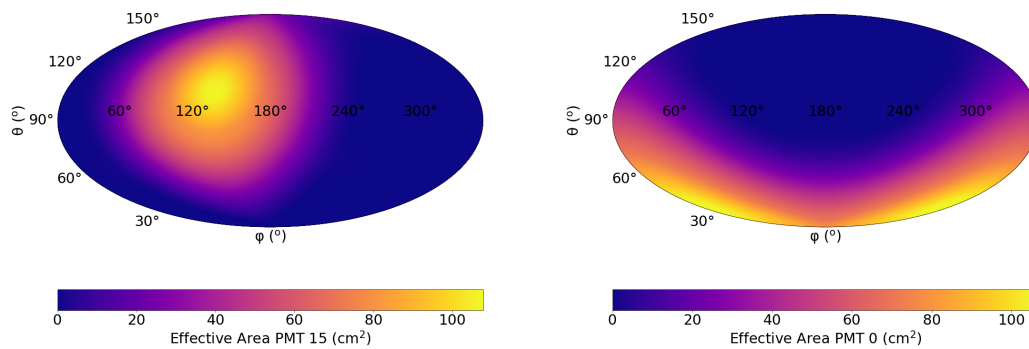


Figure 4.3: Angular effective area for two PMTs of the module without quantum efficiency for an incident plane wavefront of 470 nm. 10^7 photons were simulated per angle pair.

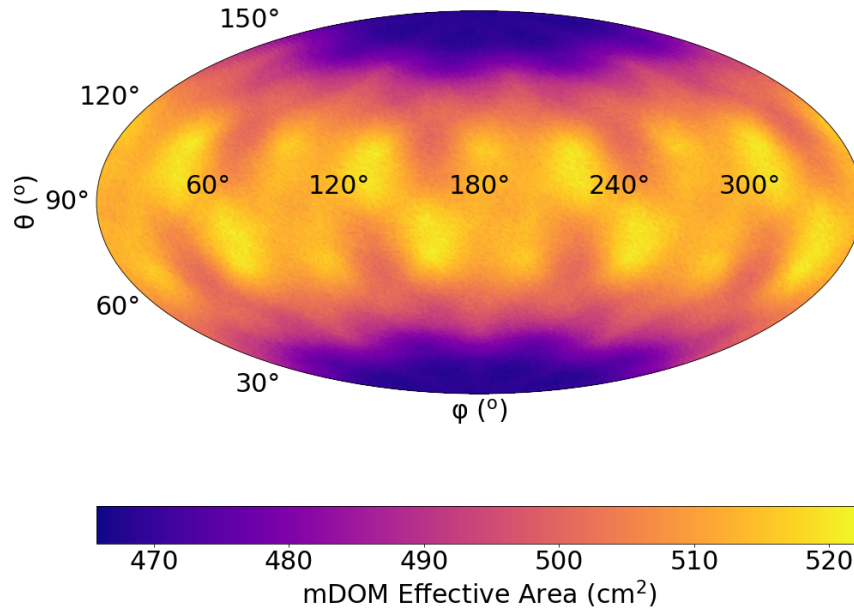


Figure 4.4: Acceptance map of the mDOM shown as the angular effective area with a near homogeneous 4π angular acceptance. The incident light has a wavelength of 390 nm which corresponds to the maximum quantum efficiency of the PMTs. 10^6 photons were simulated per angle pair. Result from [36]

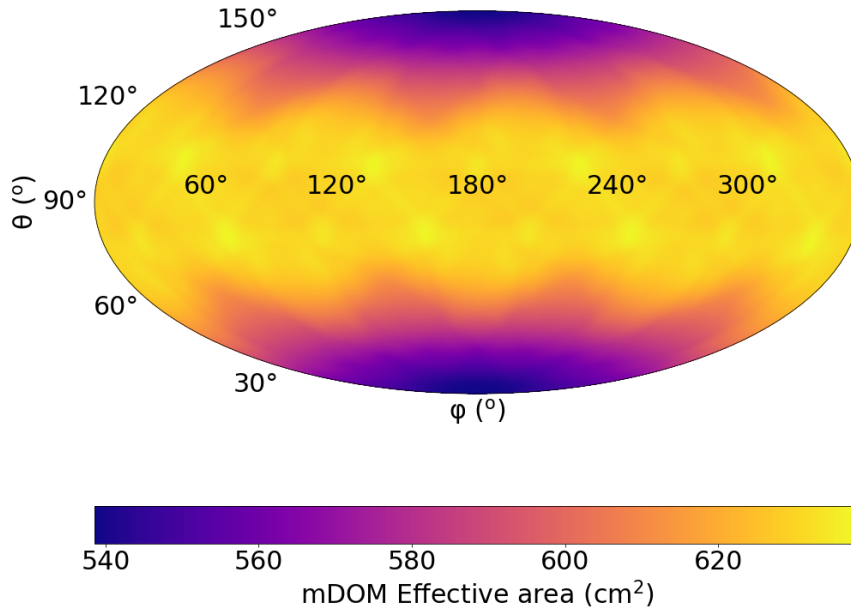


Figure 4.5: Acceptance map of the mDOM without consideration of quantum efficiency shown as the angular effective area with a near homogeneous 4π angular acceptance. The incident light has a wavelength of 470 nm. 10^7 photons were simulated per angle pair.

The inhomogeneity of the angular acceptance of the mDOM can be expressed by means of:

$$I = \frac{A_{\max} - A_{\min}}{A_{\max}}, \quad (4.2)$$

where A_{\max} is the maximum value of the effective area and A_{\min} is the minimum. The mDOM angular acceptance inhomogeneities for the first scan is $I = (10.9 \pm 0.2)\%$ where $\lambda = 390$ nm and $N_{\text{emit}} = 10^6$. For the second scan made on the mDOM $I = (15.7 \pm 0.2)\%$ where $\lambda = 470$ nm, $N_{\text{emit}} = 10^7$ and ideal PMTs were simulated ($\text{QE} = 100\%$). This difference in inhomogeneity between the two tables

can be due to the different wavelengths used and the different number of angles from which the scans were carried out. For the second tables the number of scans performed was much higher.

These scans are used for the reconstruction of the angular position of the POCAM. The POCAM was simulated as a point source of isotropic light located at distances from 20 m and above. The rays of light from a point source located 20 m away from the mDOM reach the mDOM practically as a plane wavefront. This is easily provable, the mDOM has a diameter no larger than $D = 40$ cm, therefore the maximal discrepancy between parallel rays and the rays coming from the point source located at $d = 20$ m will be:

$$\begin{aligned}\alpha &= 90^\circ - \arctan\left(\frac{d}{D/2}\right) \\ &= 90^\circ - \arctan\left(\frac{20}{0.5 \cdot 0.04}\right) = 0.057^\circ\end{aligned}\tag{4.3}$$

Hence the incident rays coming from the point source reach the mDOM almost as a plane wavefront.

4.4 Directional reconstruction of a point source

4.4.1 Initial approach

In a first approximation to the reconstruction of the angular position of the simulated POCAM, the procedure carried out in [36] is followed. Here, a two-dimensional Gaussian fit is performed around the maximum of a distribution interpreted as a proxy for a probability map of the angular position of the source. The probability for each θ, φ is obtained by:

$$P(\theta, \varphi) = \sum_{i=0}^{23} N_i \cdot S_i(\theta, \varphi).\tag{4.4}$$

This distribution $P(\theta, \varphi)$ is the sum of the angular sensitivities of each PMT, which was calculated with the scans presented in section 4.3, weighted by the

number of photons N_i recorded by the respective PMT i for a certain point source position. The light source direction is the maximum of this distribution, determined by the fit of the two-dimensional Gaussian:

$$G(\theta, \varphi) = A \cdot \exp \left[-a(\varphi - \varphi_0)^2 + 2b(\varphi - \varphi_0)(\theta - \theta_0) - c(\theta - \theta_0)^2 \right] + t, \quad (4.5)$$

where A is the amplitude of the peak, t an offset, and the information about the width of the peak and its rotation in the (θ, φ) plane is contained in the a , b and c parameters.

One of the parameters that is used for determining the goodness of the reconstruction is the opening angle. This is defined as the angle between the vector which is pointing to the real angular position of the source and the vector which is pointing to the reconstructed angular position.

The first studies were carried out for a source position at $(\theta = 90^\circ, \varphi = 180^\circ)$ and the initial scan tables of 10^6 photons of wavelength 390 nm were used [36]. The distance between the module and the point source is 20 m and a POCAM pulse of 10^9 photons is assumed. An example of the probability map and its reconstruction obtained by such a POCAM pulse is depicted in Figure 4.6. In this particular case an angular reconstruction of $\theta_{\text{Gauss}} = 91.28^\circ \pm 0.05^\circ$, $\varphi_{\text{Gauss}} = 179.56^\circ \pm 0.03^\circ$ and an opening angle $\delta = 1.36^\circ \pm 0.05^\circ$ is obtained.

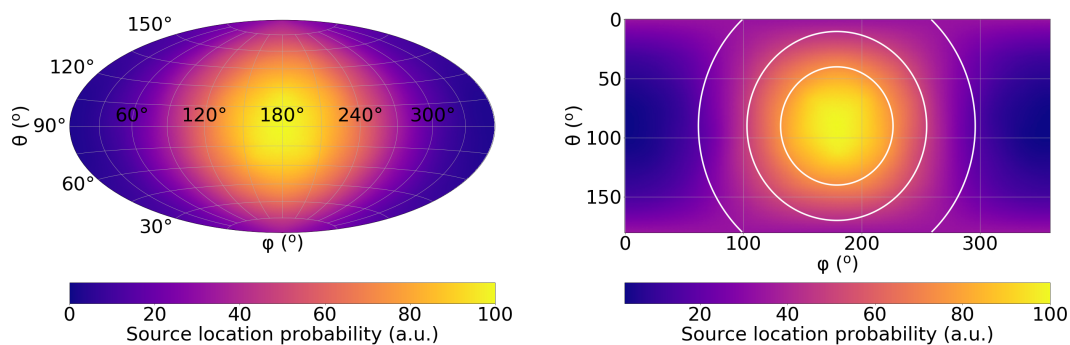


Figure 4.6: **Left:** $P(\theta, \varphi)$ distribution map of the source position. Simulated position of the source $(\theta = 90^\circ, \varphi = 180^\circ)$. **Right:** Gaussian fit around the maximum of the probability map.

This setup was repeated for a total of 1200 simulations with 10^9 photons each. The reconstruction of all these simulations results in the histograms of θ_{Gauss} , φ_{Gauss} and δ shown in Figures 4.7 and 4.8. The average of these distributions are: $\theta_{\text{Gauss}} = 90.015^\circ \pm 0.001^\circ$, $\varphi_{\text{Gauss}} = 179.954^\circ \pm 0.001^\circ$, $\delta = 1.226^\circ \pm 0.001^\circ$ and their standard deviations: $\sigma_\theta = 1.22^\circ$, $\sigma_\varphi = 0.70^\circ$ and $\sigma_\delta = 0.70^\circ$. It is noticeable that, although a single POCAM flash may not be accurate enough for the position reconstruction, several flashes lead to a correct angle average.

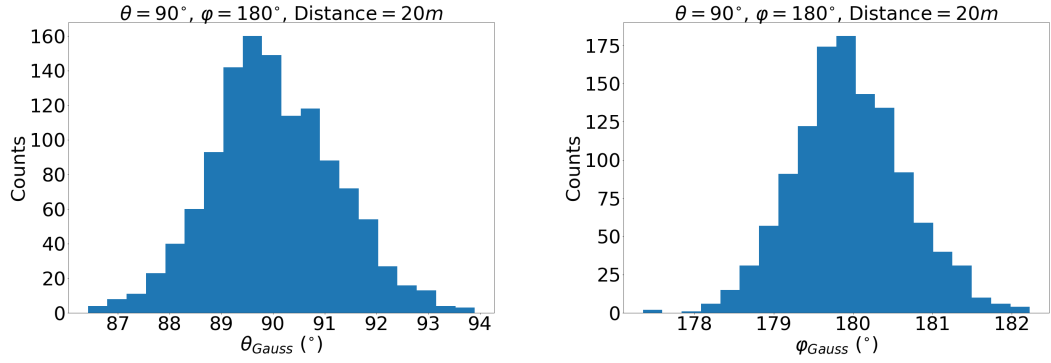


Figure 4.7: Histograms of θ (left) and φ (right) fitted gaussian values for 1200 simulations of point source when the source is placed at $(\theta = 90^\circ, \varphi = 180^\circ)$ 20 meters away from the mDOM.

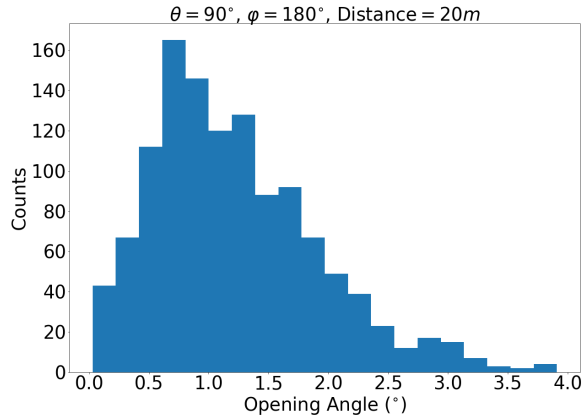


Figure 4.8: Opening angle histogram of 1200 point source simulations.

Distance effect

In order to study the influence of the source position on the reconstruction, different cases were studied. First, the angles were fixed at $(\theta = 90^\circ, \varphi = 180^\circ)$

and the simulation was carried out with the source at distances from 20 m to 80 m. For each of these distances 900 POCAM pulses were simulated with 10^9 photons each. The reconstructed angles in dependence of the distance are shown in Figure 4.9 and the opening angles in Figure 4.11. It can be observed that the uncertainty in the angular orientation of the source increases with the distance for single POCAM flashes. Notwithstanding that the opening angle mean value increase with the distance, when the Gaussian fit is performed, a precise reconstructed mean values for θ_{Gauss} and φ_{Gauss} for the angular direction of the source is obtained. Despite this, the standard deviation of these values θ_{Gauss} , φ_{Gauss} and δ increase with the distance, this can be observed in Figures 4.10 and 4.11. Reconstructed values are shown in Table 4.2. This means, that in order to have an accurate position reconstruction more POCAM flashes have to be performed for modules further away from the flasher.

Table 4.2: Mean opening angle δ and average reconstructed angles ($\theta_{\text{Gauss}}, \varphi_{\text{Gauss}}$) for 900 point source simulations placed at $(\theta, \varphi) = (90^\circ, 180^\circ)$ for different distances.

Distance (m)	θ_{Gauss} ($^\circ$)	φ_{Gauss} ($^\circ$)	Opening angle (δ) ($^\circ$)
20	89.88 ± 0.03	179.85 ± 0.02	0.913 ± 0.016
25	89.86 ± 0.04	179.86 ± 0.03	1.183 ± 0.021
30	89.94 ± 0.05	179.84 ± 0.03	1.486 ± 0.027
35	89.86 ± 0.06	179.80 ± 0.04	1.79 ± 0.03
40	89.82 ± 0.06	179.82 ± 0.05	2.03 ± 0.04
45	89.88 ± 0.08	179.99 ± 0.05	2.44 ± 0.04
50	89.88 ± 0.09	179.88 ± 0.06	2.80 ± 0.05
55	89.77 ± 0.10	179.94 ± 0.06	3.20 ± 0.06
60	89.82 ± 0.12	179.89 ± 0.08	3.68 ± 0.07
65	89.84 ± 0.12	179.97 ± 0.09	4.04 ± 0.07
70	89.96 ± 0.14	179.96 ± 0.10	4.64 ± 0.08
75	89.86 ± 0.16	179.87 ± 0.11	5.02 ± 0.09
80	89.69 ± 0.16	179.94 ± 0.12	5.36 ± 0.09

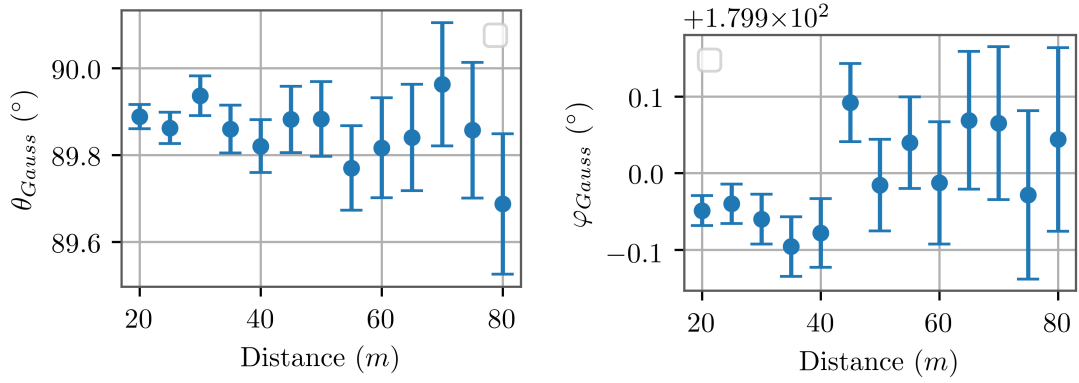


Figure 4.9: Mean reconstructed θ_{Gauss} (left) and φ_{Gauss} (right) for 900 point source simulations for different distances.

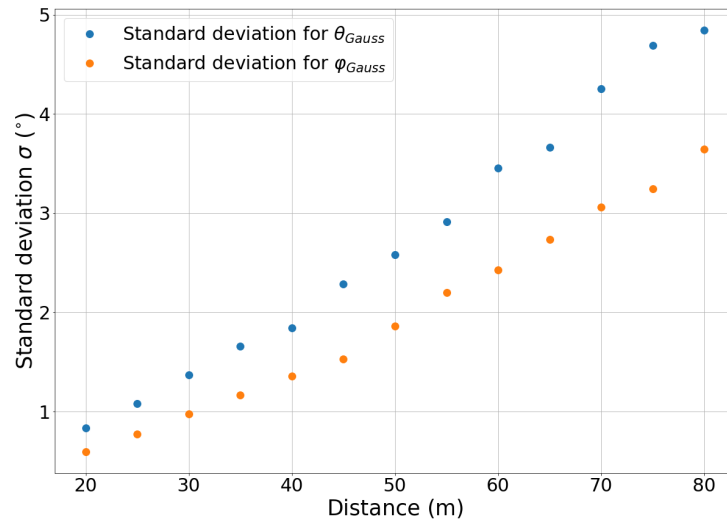


Figure 4.10: Standard deviation values for θ_{Gauss} and φ_{Gauss} for 900 point source simulations placed at $(\theta, \varphi) = (90^\circ, 180^\circ)$ at different distances.

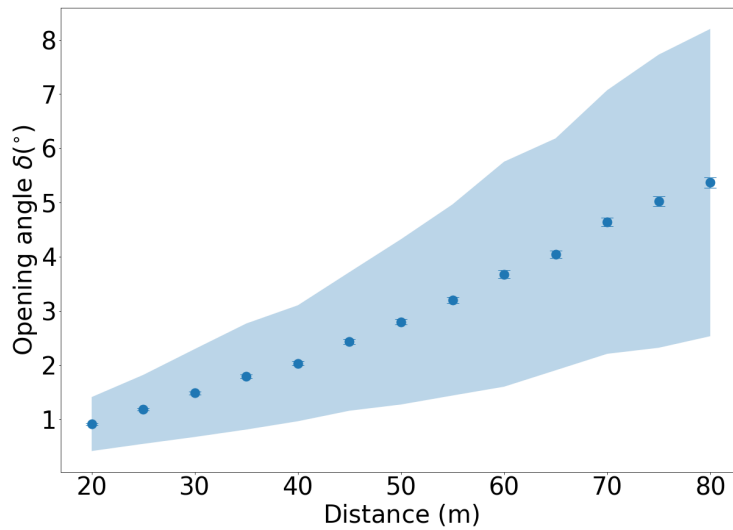


Figure 4.11: Mean opening angles values for 900 point source simulations placed at $(\theta, \varphi) = (90^{\circ}, 180^{\circ})$ at different distances. The shadow represents the standard deviation σ of these results for each distance.

Direction effect

Since the mDOM sensitivity is not distributed homogeneously for all angles, the influence of the angular position of the source was also studied, leaving the point source at a fixed distance of 20 m. 500 simulations were made for each angular position of the point source simulating 10^9 photons each. In Table 4.3 the average opening angle and reconstructed angles θ_{Gauss} and φ_{Gauss} from these 500 simulations can be found.

The point source was moved along the θ axis and φ axis. It can be observed that for variations of the angle φ keeping θ constant at $\theta = 90^{\circ}$, the reconstruction remained precise around the equator of the mDOM. Some probability maps for a single simulation moving the source around the φ axis are shown in Figure 4.12. But the opposite did not happen. When the source was moved along θ axis being $\varphi = 180^{\circ}$ the values of the reconstruction were more imprecise the further we move away from $\theta = 90^{\circ}$. These effects can be observed in Figure 4.13 where some probability maps for a single simulation are shown.

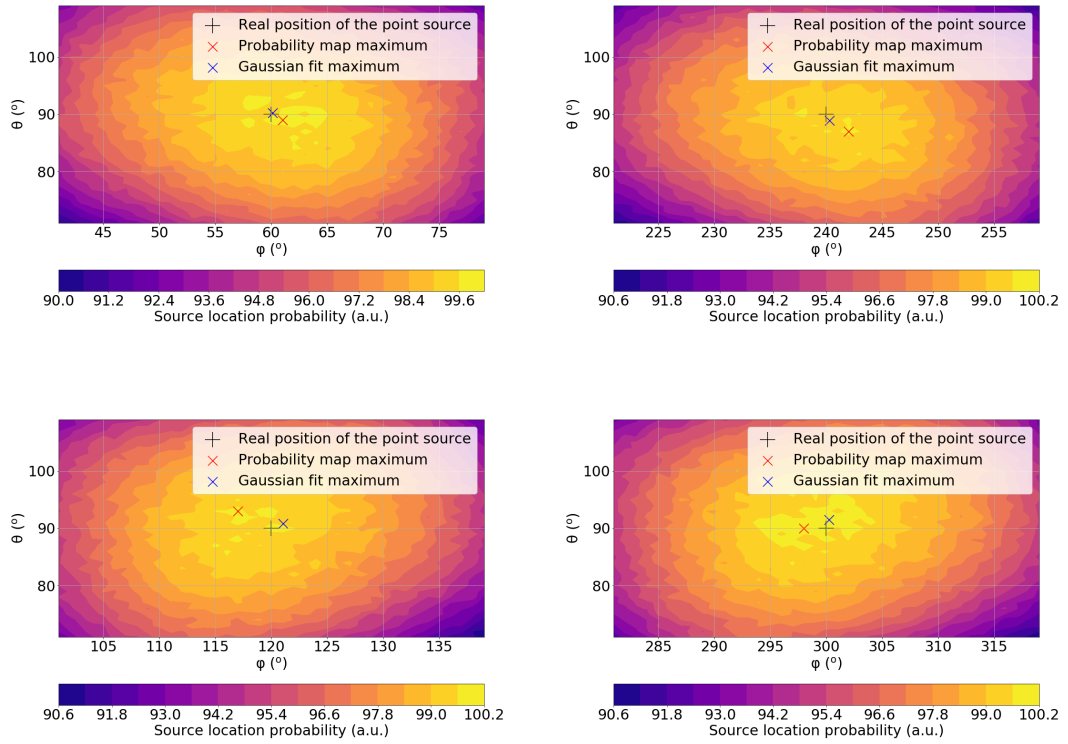


Figure 4.12: Probability map of the source position for a single point source simulation. The maximum of the probability map, the gaussian fit maximum and the real position of the source were marked. **Top:** Simulated position of the source ($\theta = 90^\circ, \phi = 60^\circ$) (left), ($\theta = 90^\circ, \phi = 240^\circ$) (right). **Bottom:** Simulated position of the source ($\theta = 90^\circ, \phi = 120^\circ$) (left), ($\theta = 90^\circ, \phi = 300^\circ$) (right).

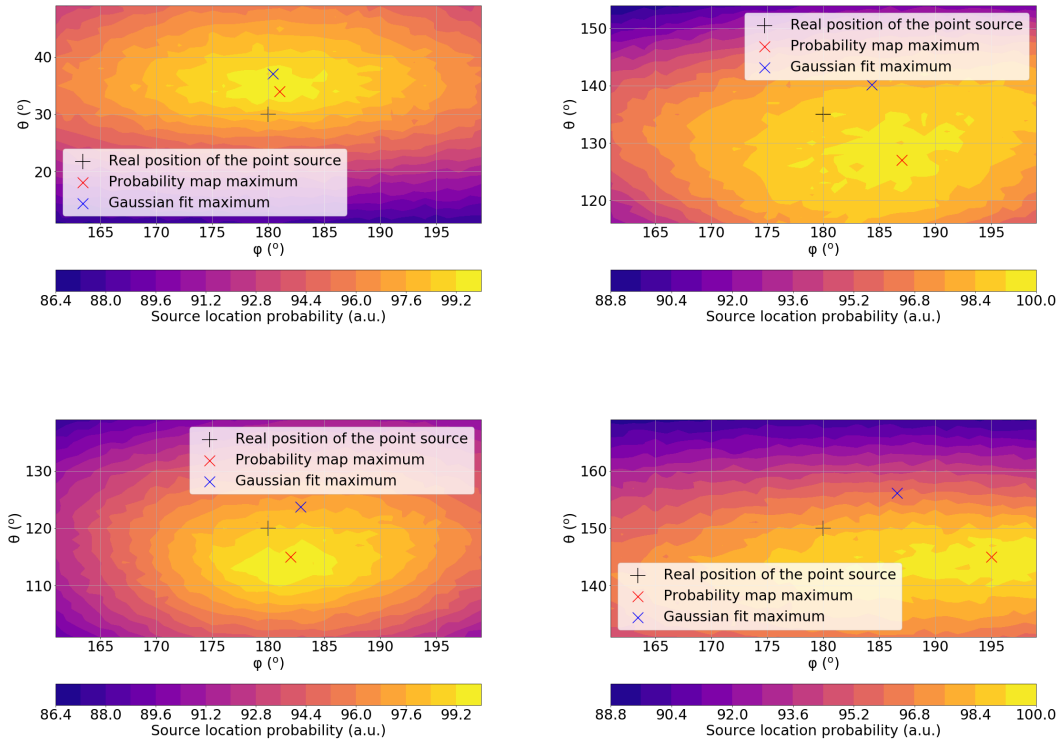


Figure 4.13: Probability map of the source position for a single point source simulation. The maximum of the probability map, the gaussian fit maximum and the real position of the source were marked. **Top:** Simulated position of the source ($\theta = 30^\circ, \varphi = 180^\circ$) (left), ($\theta = 135^\circ, \varphi = 180^\circ$) (right). **Bottom:** Simulated position of the source ($\theta = 120^\circ, \varphi = 180^\circ$) (left), ($\theta = 150^\circ, \varphi = 180^\circ$) (right).

In Figure 4.16 the opening angle δ in function of the angular position of the point source when varying φ and θ is shown. In Figures 4.14 and 4.15 the deviation of the mean θ_{Gauss} and φ_{Gauss} values respect to the real position of the source are depicted when the source is moved along φ and θ respectively. It is noticeable how the values of the standard deviation of the reconstructed angles remain practically constant despite obtaining imprecise reconstruction values. The reconstruction method used is failing when varying θ .

Angular position of the source	θ_{Gauss} ($^{\circ}$)	φ_{Gauss} ($^{\circ}$)	Opening angle (δ ($^{\circ}$))
$(\theta, \varphi) = (30^{\circ}, 180^{\circ})$	37.89 ± 0.22	180.05 ± 0.08	7.59 ± 0.03
$(\theta, \varphi) = (45^{\circ}, 180^{\circ})$	50.64 ± 0.03	180.000 ± 0.026	5.671 ± 0.028
$(\theta, \varphi) = (60^{\circ}, 180^{\circ})$	62.196 ± 0.025	180.15 ± 0.03	2.297 ± 0.02
$(\theta, \varphi) = (75^{\circ}, 180^{\circ})$	75.658 ± 0.022	180.18 ± 0.03	0.989 ± 0.022
$(\theta, \varphi) = (120^{\circ}, 180^{\circ})$	123.543 ± 0.028	182.148 ± 0.029	4.203 ± 0.024
$(\theta, \varphi) = (135^{\circ}, 180^{\circ})$	140.52 ± 0.03	183.37 ± 0.03	6.51 ± 0.03
$(\theta, \varphi) = (150^{\circ}, 180^{\circ})$	156.82 ± 0.03	183.14 ± 0.04	7.54 ± 0.03
$(\theta, \varphi) = (90^{\circ}, 0^{\circ})$	89.90 ± 0.04	0.537 ± 0.018	1.018 ± 0.022
$(\theta, \varphi) = (90^{\circ}, 60^{\circ})$	90.05 ± 0.04	60.617 ± 0.020	1.006 ± 0.022
$(\theta, \varphi) = (90^{\circ}, 120^{\circ})$	90.10 ± 0.04	120.548 ± 0.018	1.045 ± 0.024
$(\theta, \varphi) = (90^{\circ}, 180^{\circ})$	90.04 ± 0.04	179.924 ± 0.022	1.235 ± 0.023
$(\theta, \varphi) = (90^{\circ}, 240^{\circ})$	89.99 ± 0.04	240.623 ± 0.020	0.998 ± 0.023
$(\theta, \varphi) = (90^{\circ}, 300^{\circ})$	90.12 ± 0.04	300.571 ± 0.019	0.997 ± 0.024
$(\theta, \varphi) = (90^{\circ}, 360^{\circ})$	90.01 ± 0.04	360.551 ± 0.019	1.027 ± 0.024

Table 4.3: Opening angle, θ_{Gauss} , φ_{Gauss} mean values for different angular positions of the source. 500 POCAM flashers were simulated for each angular position.

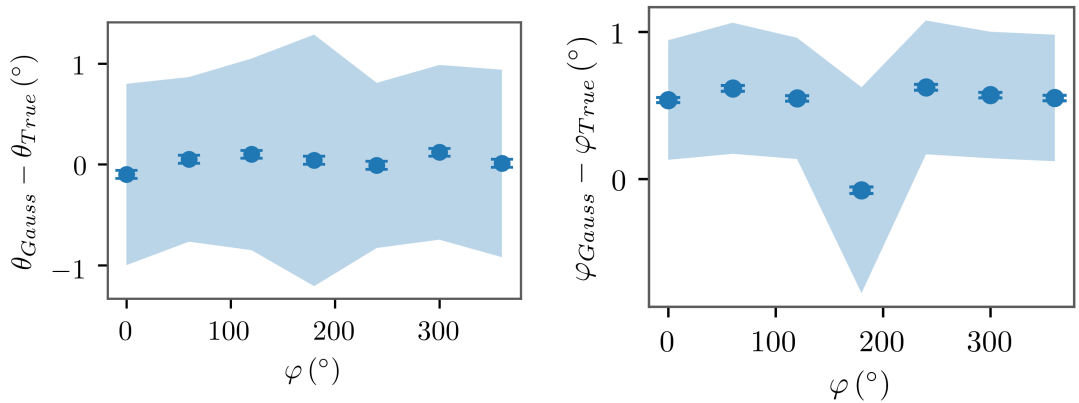


Figure 4.14: Deviation of the mean θ_{Gauss} values respect to the real position θ_{True} (left) and Deviation of the mean φ_{Gauss} values respect to the real position φ_{True} (right) of the source when varying coordinate φ . The shadow represents the standard deviation σ

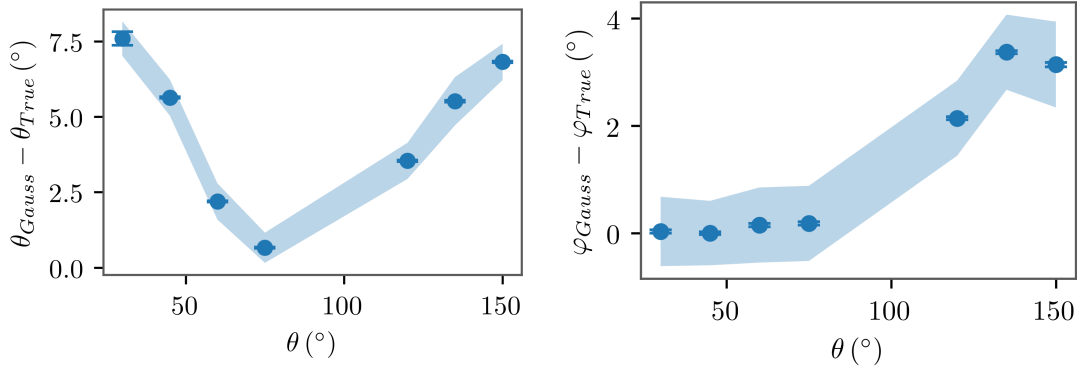


Figure 4.15: Deviation of the mean θ_{Gauss} values respect to the real position θ_{True} (left) and Deviation of the mean φ_{Gauss} values respect to the real position φ_{True} (right) of the source when varying coordinate θ . The shadow represents the standard deviation σ

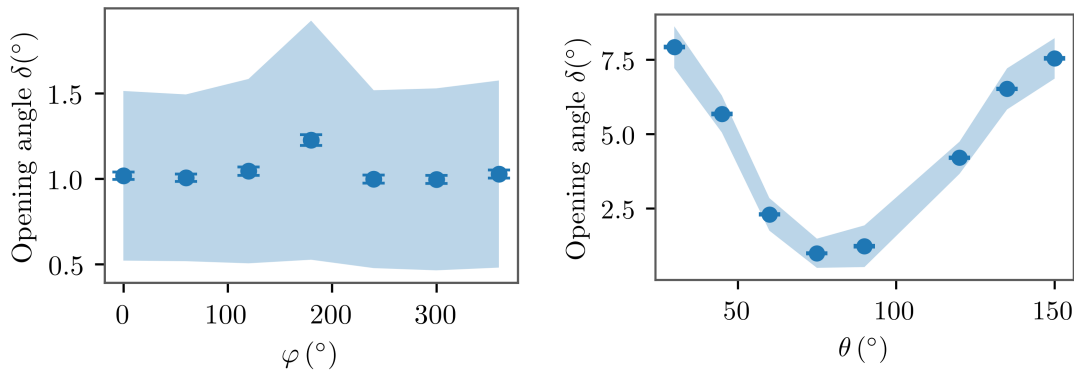


Figure 4.16: Mean opening angles values when the source is moved around φ axis (left) and θ axis (right). The shadow represents the standard deviation σ of these opening angles. The reconstruction is inaccurate when θ is varied.

The reconstruction did not improve by increasing the statistics assuming larger POCAM flashes. Hits of different simulations were added together to decrease the statistical noise but same results were obtained: An accurate reconstruction when varying φ but an inaccurate one when θ is changed. All Gaussian shapes in the probability maps for different angular positions of the source are displaced towards $\theta = 90^{\circ}$ of the mDOM when the θ position of the source is varied as it is depicted in Figure 4.17.

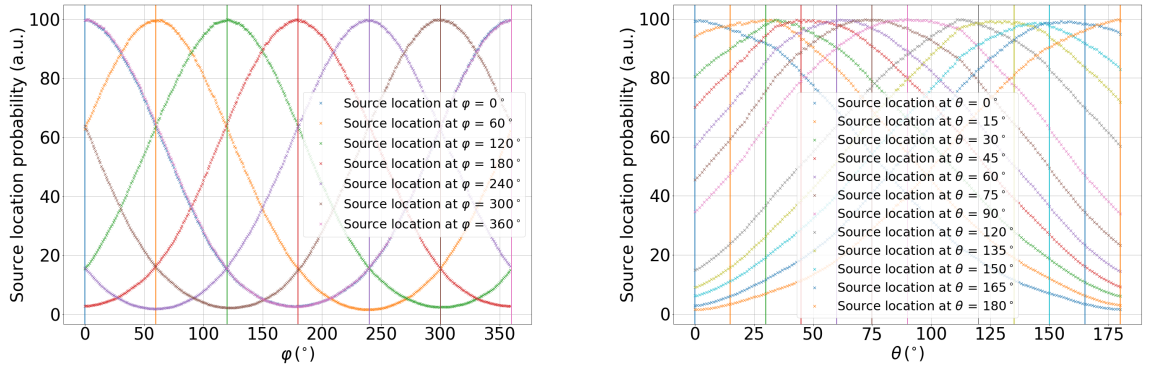


Figure 4.17: Left: Cuts in the probability maps for $\theta = 90^\circ$ and different values of the source in φ . **Right:** Cuts in the probability map for $\varphi = 180^\circ$ and different values of the source in θ . It is noticeable how, varying θ , the probability maps are moved slightly towards $\theta = 90^\circ$ which corresponds to the equator of the mDOM.

To verify that this effect is not related to the distance between the module and the source, a study was made at different distances in which the source was located in $\theta = 30^\circ, \varphi = 180^\circ$. 1216 POCAM flashes of 10^9 photons were simulated for each distance. The selected distances were 10, 20, 50 and 100 m. The number of hits in these 1216 simulations were added for each PMT to decrease the statistical noise, equaling the simulation of a single POCAM flash of $\sim 10^{12}$ photons. The θ_{Gauss} , φ_{Gauss} and opening angle values calculated are shown in Table 4.4.

Distance (m)	θ_{Gauss} ($^\circ$)	φ_{Gauss} ($^\circ$)	Opening angle (δ ($^\circ$))
10	36.44 ± 0.03	180.26 ± 0.03	6.45 ± 0.03
20	36.56 ± 0.03	180.15 ± 0.03	6.55 ± 0.03
50	36.94 ± 0.03	180.87 ± 0.03	6.99 ± 0.03
100	36.41 ± 0.03	183.01 ± 0.04	7.08 ± 0.03

Table 4.4: θ_{Gauss} and φ_{Gauss} values for the Gaussian fit and opening angle δ for point source simulations placed at $(\theta, \varphi) = (30^\circ, 180^\circ)$ at different distances.

These results verify that the distance between module and source does not play any relevant role concerning this problem since Gaussians are always displaced towards the equator of the mDOM as one can see in Figures 4.18 and 4.19.

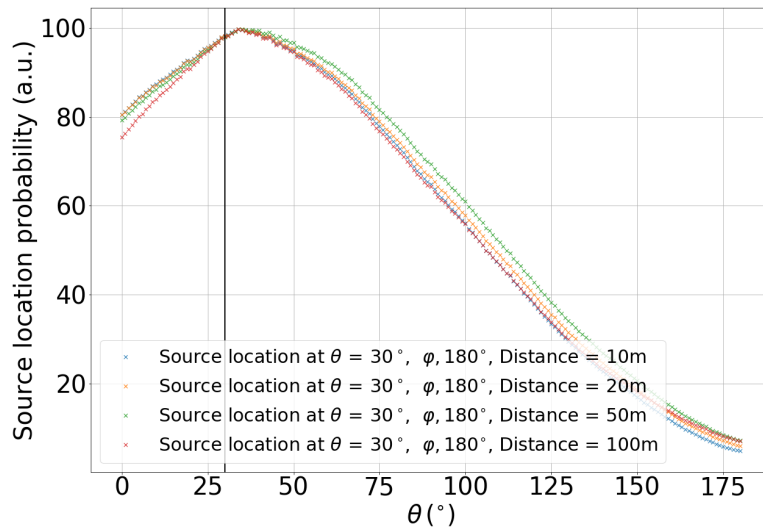


Figure 4.18: Source location probabilities for a point source placed at $(\theta, \varphi) = (30^{\circ}, 180^{\circ})$ for different distances between the source and the module. The distance does not affect the movement of the maximum of the probability towards the equator of the mDOM.

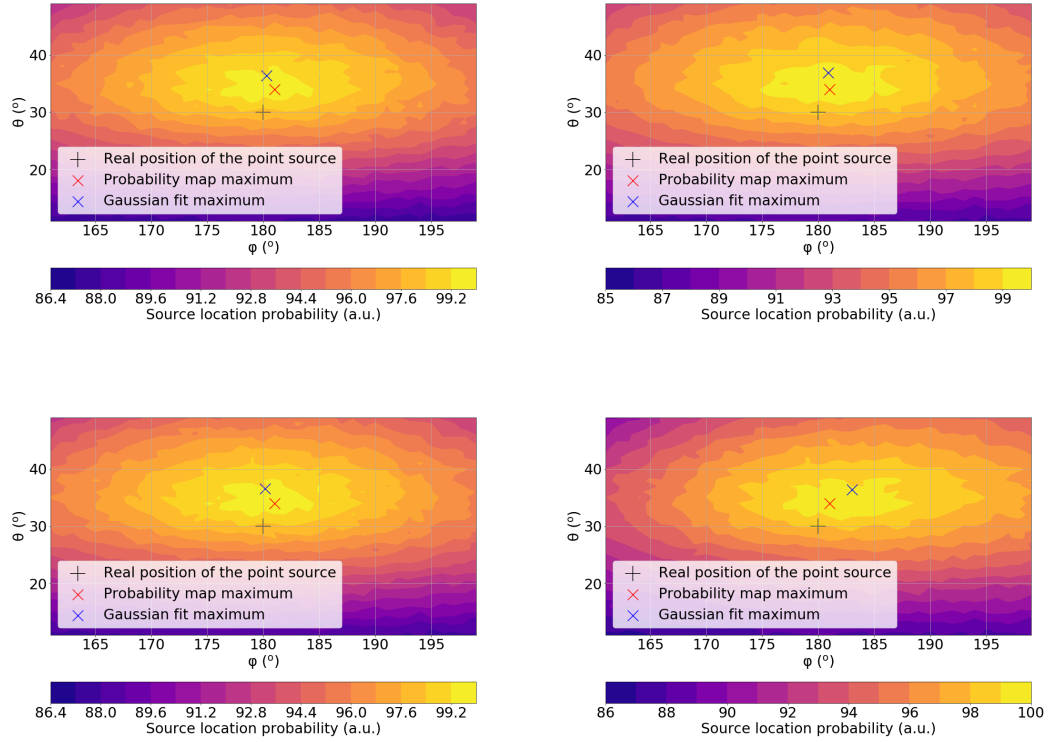


Figure 4.19: Probability map of the source position for different distances. Simulated position of the source ($\theta = 30^\circ, \varphi = 120^\circ$). The maximum of the probability map, the gaussian fit maximum and the real position of the source were marked. **Top:** Distance 10 m (left), distance 20 m (right). **Bottom:** Distance 50 m (left), distance 100 m (right).

The explanation for these deviations is found in the small inhomogeneities of the mDOMs angular acceptance (Fig. 4.40). The angular acceptance is higher at the equator, where there is a higher PMT density. Because of this and the reconstruction method used, the probability distributions are shifted towards $\theta = 90^\circ$ since we do not compare how similar the number of hits are between the scans and our point sources simulations but we consider that an angular position is more probable the higher its $P(\theta, \varphi)$ is. For this reason, and to achieve a better precision in the reconstruction the Maximum likelihood method will be used instead of equation 4.4. The results are presented in the next section.

4.4.2 Likelihood reconstruction

Maximum likelihood estimation is a statistical method in which given a data sample x_1, \dots, x_N , it attempts to find the parameter values that maximize the likelihood function.

The Likelihood function for N parameters is defined as [40]:

$$L(x_1, \dots, x_N; \mu_1, \dots, \mu_N) = \prod P(x_i, \mu_i), \quad (4.6)$$

which is transformed to make it easier to be treated mathematically:

$$\mathcal{L} = \log(L(x_1, \dots, x_N; \mu_1, \dots, \mu_N)) = \sum \log(P(x_i, \mu_i)), \quad (4.7)$$

being x_i the value of the registered hits in the PMT i for a certain angular position of the source and μ_i the expected value from the scans for that PMT. The function $P(x_i, \mu_i)$ is called probability mass function. For the studies of this work the probability mass function is taken as a Gaussian distribution when the expected value of the number of hits in a certain PMT is higher than 20 ($\mu_i > 20$). Thus, the probability of obtaining x_i hits in the PMT when the expected number is μ_i :

$$P(x, \mu > 20, \sigma^2 = \mu) = \frac{1}{\sigma\sqrt{2\pi}} \cdot e^{-\frac{x-\mu^2}{2\sigma^2}}. \quad (4.8)$$

However, when the expected value in the number of hits for a certain PMT is lower or equal to 20 ($\mu_i \leq 20$) a Gaussian distribution is not appropriate to describe the probability distribution and the Poissonian distribution must be used:

$$P(x, \mu \leq 20) = \frac{e^{-\mu} \cdot \mu^x}{x!}. \quad (4.9)$$

For the studies, the interest lies in the hit distribution around the mDOM and not in the total number of hits, therefore and to be able to use the approach explained before, a factor F is used to normalized the results with the total number of hits:

$$F = \frac{\sum x_i}{\sum \mu_i}. \quad (4.10)$$

So now μ will be $\mu = \mu/F$. The reconstructed values of θ and φ corresponding to the most likely angular direction where the source is found are given by the corresponding maximum value of the likelihood function. The uncertainty for these θ and φ values is defined via the cumulative distribution function.

The cumulative distribution function *CDF* for the Likelihood method used in the reconstruction of the angular position of the source can be calculated via:

$$CDF = \frac{1}{\Gamma(k/2)} \cdot \gamma\left(\frac{k}{2}, \frac{x}{2}\right), \quad (4.11)$$

where Γ is the Gamma function, γ is the lower incomplete gamma function and k is the degrees of freedom. There are 24 different PMTs and two coordinates, θ and φ , thus the number of degrees of freedom of the system is $k = 24 - 2 = 22$. This way the cumulative distribution function for the system can be calculated and its represented in Figure 4.22. Where $\gamma(11) = 10!$ and $\gamma(11, \frac{x}{2}) = \int_0^{x/2} t^{10} \cdot e^{-t} dt$. The σ region for our system is obtained by means of $CDF(2 \cdot (\ln L - \ln L_{Max})) = 0.6827$ which leads to $2 \cdot (\ln(L) - \ln(L_{Max})) = -24.59$ and the 2σ region by $CDF(2 \cdot (\ln L - \ln L_{Max})) = 0.9545$ which leads to $2 \cdot (\ln(L) - \ln(L_{Max})) = -34.33$.

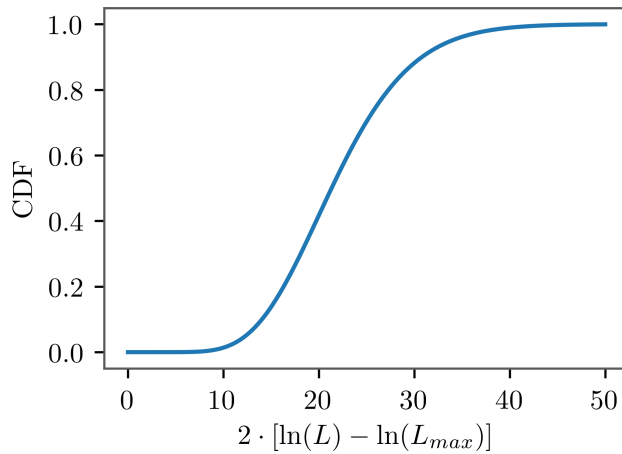


Figure 4.20: Cumulative distribution function for the Likelihood method.

Some changes had to be carried out so that the Maximum Likelihood method worked correctly. If the expected value for a certain PMT is zero and in the point source simulation this PMT registers some hits, the information of that direction would be lost, since the probability from Poisson would be zero and therefore

the logarithm $-\inf$, failing the math in this case. Therefore, if a certain PMT registers zero hits in the scan for a certain direction, this value is changed to one. This was tested to be a good approach and should not be necessary when more photons are simulated in the scans.

In the initial approach using the Maximum likelihood estimation and the first scan described in 4.3 it was possible to verify how now the Gaussian shapes are now centered around the correct value, which correct the effect saw using the method of section 4.4.1. Also, the shapes of the likelihood distribution of are now much narrower, leading to a better resolution. See Figure 4.21. Hits for 1000 simulations were added to decrease the statistical noise equaling, as previously, the simulation of a single POCAM pulse of $\sim 10^{12}$ photons.

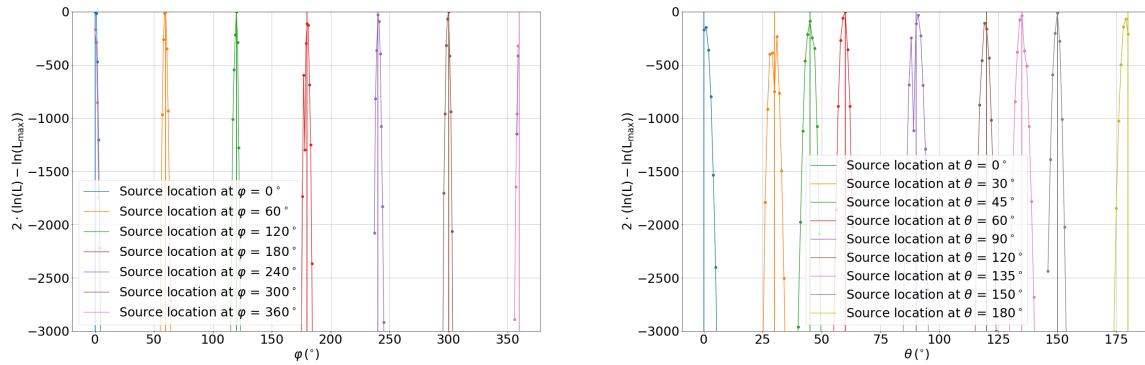


Figure 4.21: Cuts in the Likelihood maps where the maximum is not shifted. **Left:** $\theta = 90^\circ$ and different angular positions of the source for φ . **Right:** $\varphi = 180^\circ$ and different angular positions of the source for θ .

Directional reconstruction using tables equally distributed along the sphere

For the first scan made over the mDOM (section 4.3), angular positions were taken varying degree by degree in both θ and φ collecting a total of 65160 plane wave simulations. In this configuration the density of points in the poles of a sphere is much higher than in the equator so the number of plane wave simulations at the equator is lower. To improve the reconstruction new scans were made on the mDOM taking homogeneous points on a sphere surface and increasing the statistic by taking more angular positions with more photons per simulation

to improve the accuracy of the reconstruction of the source. In total 786432 plane wave simulations were performed on the mDOM from points that obey the condition of homogeneity in a sphere surface. To generate such a quantity of homogeneous points the HEALPix¹ software [41] was used. The pixelization produces a subdivision of a spherical surface in which each pixel covers the same surface area as every other pixel. In each simulation 10^7 photons are simulated from a plane disc towards the mDOM, ten times more than in the previous scan, reducing the statistical noise. The angular distance between two pixels used for the scans is less than 0.4° and hence this is the new precision of the reconstruction method presented in this section. The precision of the previous scan was 1° . From now on, for the reconstruction of the point source simulation, the scans performed with HEALPix were used.

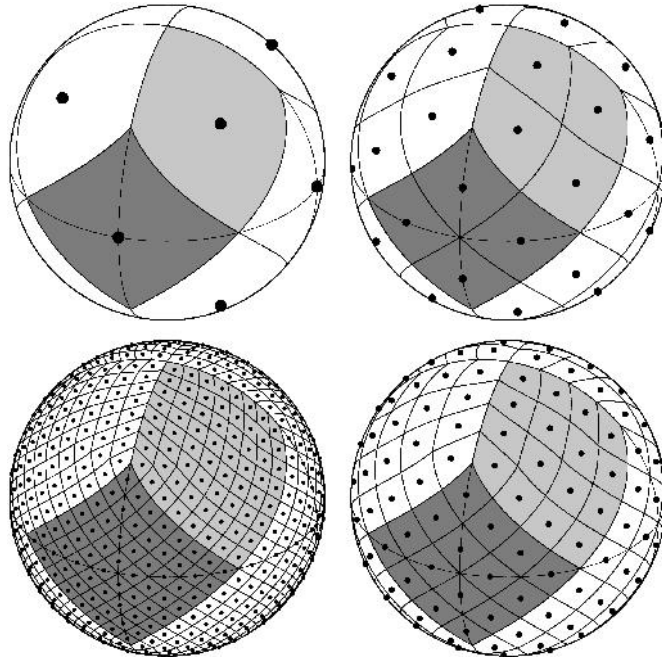


Figure 4.22: Healpix distribution of points around the spherical coordinates θ and ϕ for different number of pixels. Figure taken from [41]

A self-consistency test is carried out for the new scans using HEALPix. Here we will compare the table with itself, including the expected statistical fluctuation. In order to do this, some angular positions of the scans were selected, and for these the hits are re-scaled to the expected values for a point source of 10^9 photons placed at 20 m . These point source simulations have an average value of 6420 total hits. After the re-scaling process and before proceeding with the likeli-

¹Acronym for Hierarchical Equal Area isoLatitude Pixelization of a sphere

hood estimator for the picked scan for a certain angular configuration, a sampling from a Poissonian distribution is obtained using μ as the different hits collected in each PMT, in order to include the statistical fluctuation that is expected in a real detection. 500 self-consistency tests were made for each selected angular configuration of the scan. In Table 4.5 the mean opening angles and the standard deviation are shown for the selected directions. These standard deviations show an uncertainty that comes from a purely statistical effect. These results indicate that the scans are a good model with which to compare the point source simulations. These results in the angular reconstruction will be compared later with point source simulations to compare the uncertainties coming from purely statistical effects as well as the uncertainties introduced by the ice in the point source simulations in the reconstruction of the source.

Table 4.5: Mean opening angle for 500 self-consistency tests for different incident angular directions of the plane wavefront. The uncertainty comes from a purely statistical effect when applying Poisson on the re-scaled hits in each PMT.

Angular direction of the plane wavefront	Opening angle (δ (°))	Standard deviation σ
$(\theta, \varphi) = (15^\circ, 180^\circ)$	0.536 ± 0.013	0.30
$(\theta, \varphi) = (30^\circ, 180^\circ)$	0.578 ± 0.014	0.30
$(\theta, \varphi) = (60^\circ, 180^\circ)$	0.637 ± 0.015	0.34
$(\theta, \varphi) = (90^\circ, 180^\circ)$	0.661 ± 0.016	0.37
$(\theta, \varphi) = (165^\circ, 180^\circ)$	0.530 ± 0.012	0.27
$(\theta, \varphi) = (90^\circ, 120^\circ)$	0.648 ± 0.016	0.35

Like in section 4.4.1, the maximum likelihood estimation is initially performed to reconstruct the angular direction of point sources placed at 20 m in an angular position $(\theta = 90^\circ, \varphi = 180^\circ)$. The probability map obtained using the maximum likelihood method is depicted in Figure 4.23. The maximum of the probability map indicate the most likely angular position of the source $(\theta_{\text{Likelihood}}, \varphi_{\text{Likelihood}})$. For an example point source simulation the following reconstruction results were obtained: $\theta_{\text{Likelihood}} = 88.8^\circ \pm 0.4^\circ$, $\varphi_{\text{Likelihood}} = 179.8^\circ \pm 0.4^\circ$ and an opening angle $\delta = 1.2^\circ \pm 0.4^\circ$. The reconstruction of 1000 simulated POCAM flashes with 10^9 photons each results in the histograms of $\theta_{\text{Likelihood}}$, $\varphi_{\text{Likelihood}}$ and δ are shown in Figures 4.24 and 4.25.

The average value for these distributions are: $\theta_{\text{Likelihood}} = 89.876^\circ \pm 0.019^\circ$,

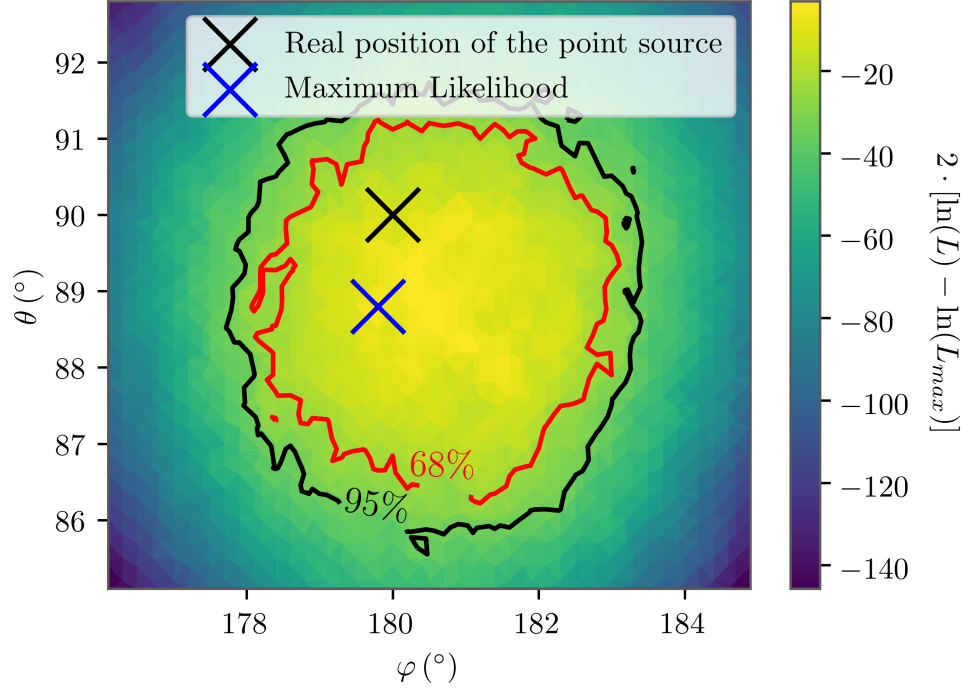


Figure 4.23: Likelihood map for a single point source simulations at 20 m and $(\theta = 90^\circ, \varphi = 180^\circ)$. The σ region is bounded by the red line and the 2σ region by the black line.

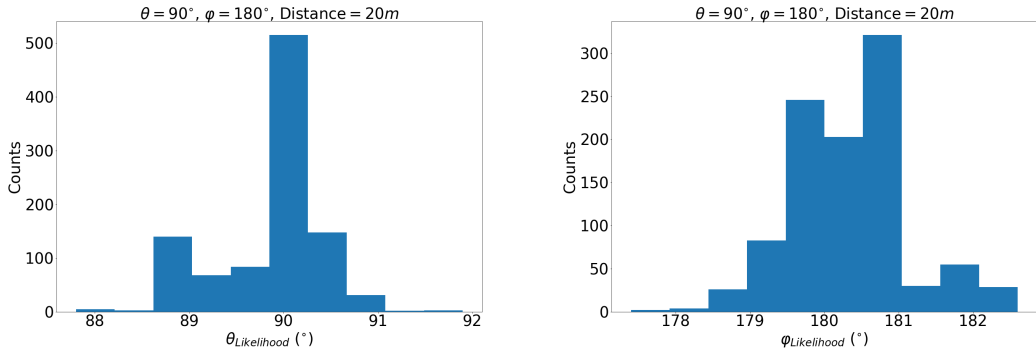


Figure 4.24: Histogram of $\theta_{\text{Likelihood}}$ (left) and $\varphi_{\text{Likelihood}}$ (right) reconstructed values for 1000 point source simulations at 20 m and $(\theta = 90^\circ, \varphi = 180^\circ)$.

$\varphi_{\text{Likelihood}} = 180.409^\circ \pm 0.025^\circ$ and $\delta = 0.953^\circ \pm 0.015^\circ$ and their standard deviations: $\sigma_\theta = 0.19^\circ$, $\sigma_\varphi = 0.25^\circ$ and $\sigma_\delta = 0.15^\circ$. Comparing these results with those obtained in 4.4.1 using the previous method where $\sigma_\theta = 1.22^\circ$, $\sigma_\varphi = 0.70^\circ$ and $\sigma_\delta = 0.70^\circ$, It is observed that using the likelihood reconstruction, the standard deviations are much smaller than with the method used in section 4.4.1. The

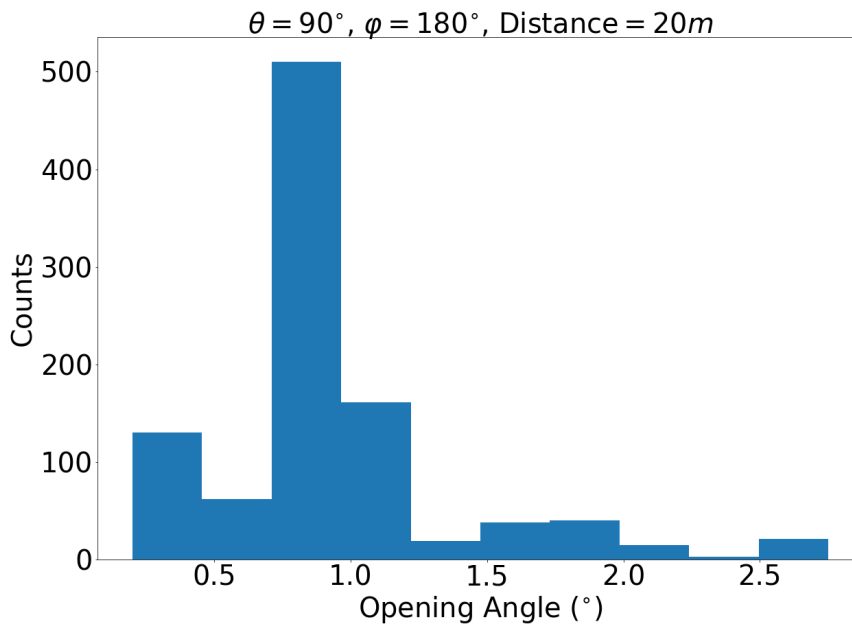


Figure 4.25: Histogram of opening angles δ values for 1000 point source simulations at 20 m and $(\theta = 90^\circ, \varphi = 180^\circ)$.

reconstruction of a POCAM flash is more accurate with the likelihood method and fewer flashes would be necessary in order to calculate the direction of the source.

Direction effect

The study was expanded to more angular positions of the source performing 1000 simulations for each angular configuration. The reconstructed mean values of the angular positions of the source using likelihood method and their opening angles are shown in Table 4.6. These results are also depicted in Figure 4.26 when the source is moved varying φ and Figure 4.27 when it is moved varying θ . The mean opening angles for both studies are depicted in Figure 4.28.

It can be observed that by means of the maximum likelihood estimation the reconstruction of the angular position of the source is accurate when varying both θ and φ and thus that the problem with θ variation was solved. The standard deviations are practically constants for both $\theta_{\text{Likelihood}}$ and $\varphi_{\text{Likelihood}}$ when varying φ . When varying θ the standard deviations for $\theta_{\text{Likelihood}}$ are practically constants but for $\varphi_{\text{Likelihood}}$ some larger values for θ values corresponding to the pole regions

Table 4.6: Mean opening angles δ , $\theta_{\text{Likelihood}}$ and $\varphi_{\text{Likelihood}}$ for different angular positions of the source. 1000 simulations were run for each angular position.

Angular source position	$\theta_{\text{Likelihood}}(^{\circ})$	$\varphi_{\text{Likelihood}}(^{\circ})$	Opening angle $\delta (^{\circ})$
$(\theta, \varphi) = (15^{\circ}, 180^{\circ})$	14.378 ± 0.014	179.66 ± 0.09	0.857 ± 0.019
$(\theta, \varphi) = (30^{\circ}, 180^{\circ})$	29.874 ± 0.023	180.09 ± 0.06	1.123 ± 0.015
$(\theta, \varphi) = (45^{\circ}, 180^{\circ})$	44.736 ± 0.019	179.9 ± 0.04	0.915 ± 0.016
$(\theta, \varphi) = (60^{\circ}, 180^{\circ})$	59.957 ± 0.014	179.747 ± 0.012	0.405 ± 0.014
$(\theta, \varphi) = (75^{\circ}, 180^{\circ})$	74.048 ± 0.022	179.926 ± 0.020	1.184 ± 0.019
$(\theta, \varphi) = (90^{\circ}, 180^{\circ})$	89.876 ± 0.019	180.409 ± 0.025	0.953 ± 0.015
$(\theta, \varphi) = (120^{\circ}, 180^{\circ})$	120.621 ± 0.016	180.087 ± 0.016	0.725 ± 0.017
$(\theta, \varphi) = (135^{\circ}, 180^{\circ})$	135.787 ± 0.023	180.190 ± 0.027	1.081 ± 0.019
$(\theta, \varphi) = (150^{\circ}, 180^{\circ})$	148.49 ± 0.04	180.45 ± 0.05	1.953 ± 0.020
$(\theta, \varphi) = (165^{\circ}, 180^{\circ})$	165.398 ± 0.021	179.91 ± 0.04	0.519 ± 0.020
$(\theta, \varphi) = (90^{\circ}, 0^{\circ})$			0.886 ± 0.017
$(\theta, \varphi) = (90^{\circ}, 60^{\circ})$	90.139 ± 0.020	59.929 ± 0.023	0.868 ± 0.014
$(\theta, \varphi) = (90^{\circ}, 120^{\circ})$	89.875 ± 0.017	119.692 ± 0.017	0.719 ± 0.014
$(\theta, \varphi) = (90^{\circ}, 240^{\circ})$	90.145 ± 0.023	239.950 ± 0.018	0.845 ± 0.012
$(\theta, \varphi) = (90^{\circ}, 300^{\circ})$	89.884 ± 0.021	299.619 ± 0.018	0.863 ± 0.013
$(\theta, \varphi) = (90^{\circ}, 360^{\circ})$			0.871 ± 0.017

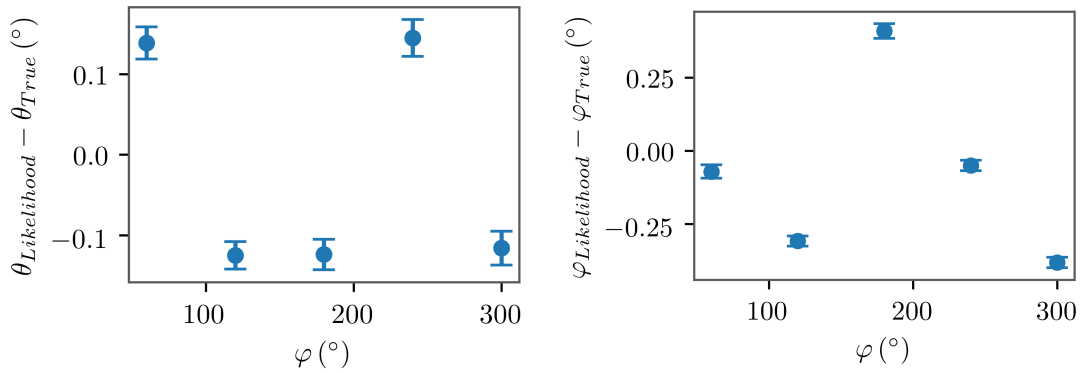


Figure 4.26: Deviation of the mean $\theta_{\text{Likelihood}}$ values respect to the real position θ_{True} (left) and Deviation of the mean φ_{Gauss} values respect to the real position φ_{True} (right) of the source when varying coordinate φ .

of the mDOM. These effects can be observed in Figure 4.29.

Figure 4.30 shows a comparison between the opening angles obtained from the

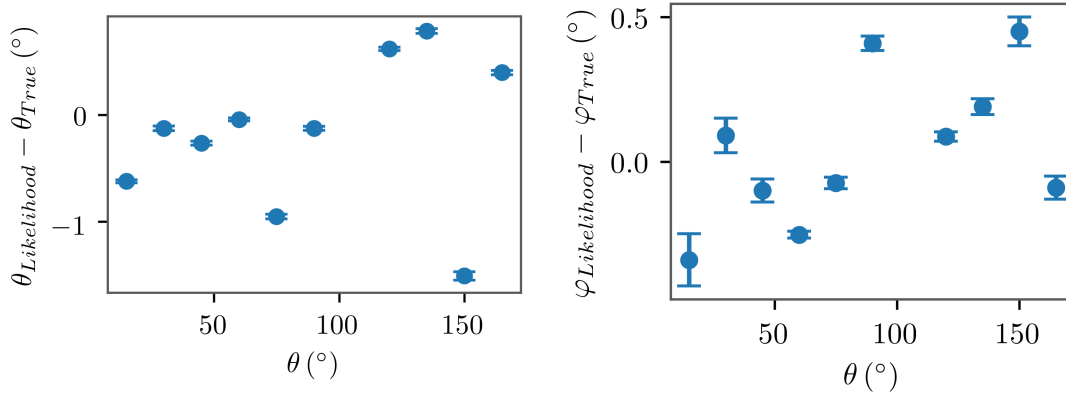


Figure 4.27: Deviation of the mean $\theta_{Likelihood}$ values respect to the real position θ_{True} (left) and Deviation of the mean φ_{Gauss} values respect to the real position φ_{True} (right) of the source when varying coordinate θ .

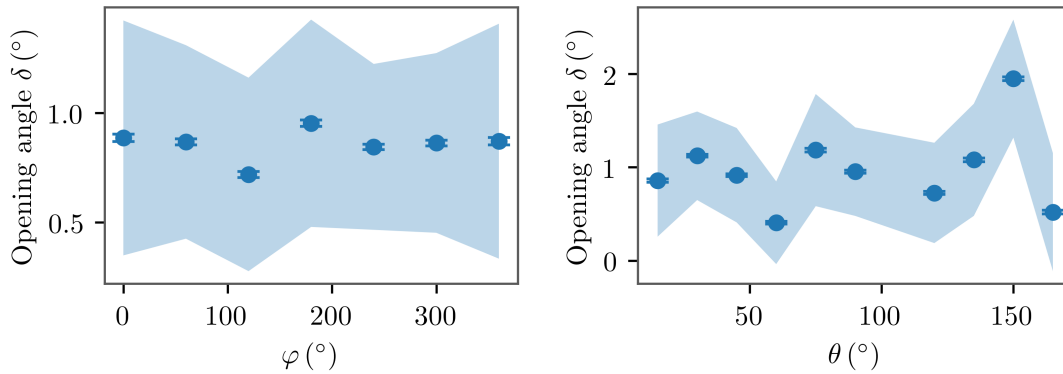


Figure 4.28: Mean opening angles values when the source is moved around φ axis (left) and θ axis (right). The shadow represents the standard deviation σ of these opening angles.

reconstruction of the simulated point source and the results of the self-consistency test from Table 4.5.

The average values of the opening angles calculated for the point source simulations are in ranges very similar to those obtained in the self-consistency method. The standard deviation of the opening angle distribution is slightly higher in the case of point source simulations. Obviously the precision is better in the self-consistency test because in the point source simulation there are the effects of absorption and scattering of photons are present, which adds a systematic error to the statistical uncertainty. It can be inferred that scans made on the mDOM are an accurate model with which to compare for reconstructions of point source sim-

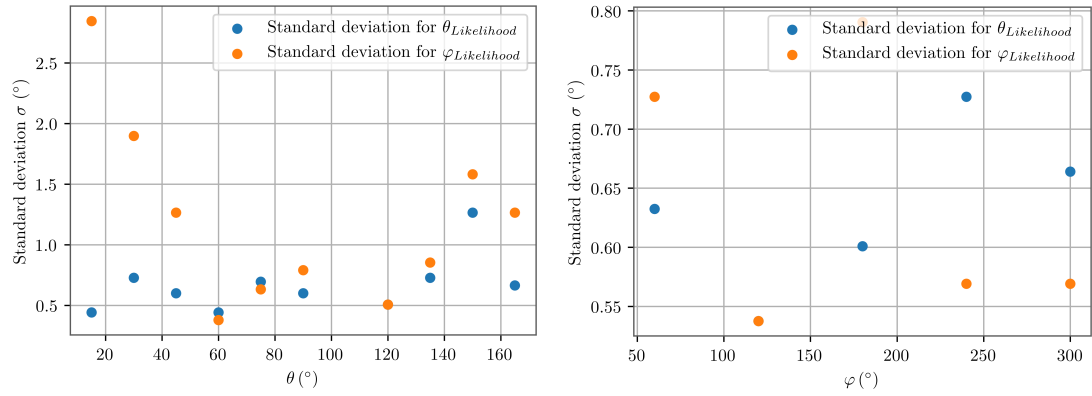


Figure 4.29: Standard deviations of reconstructed values when the source is moved around θ axis (left) and φ axis (right).

ulations. Although the sensitivity of the mDOM is not completely homogeneous at all angles, there are no noticeable effects in the reconstruction by changing the angular position of the POCAM.

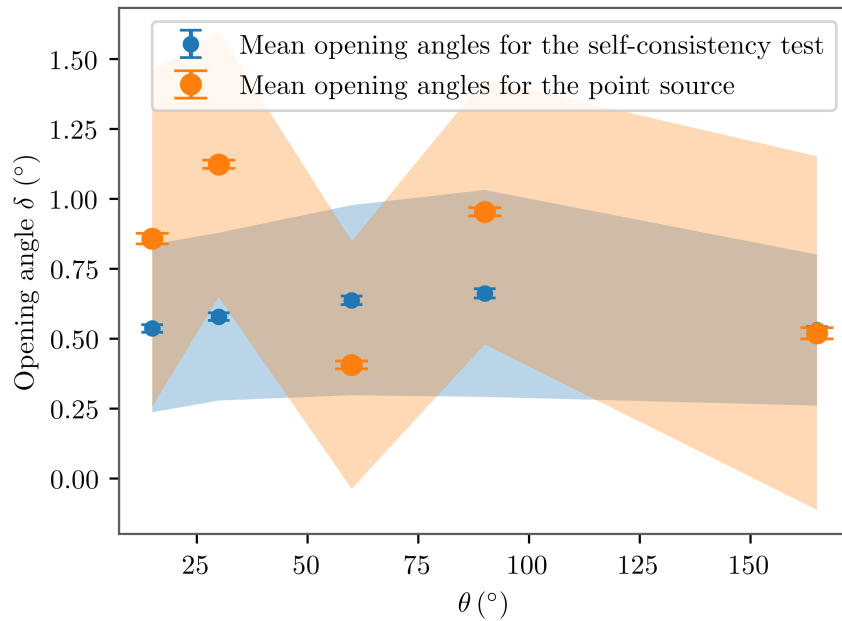


Figure 4.30: Mean opening angles for 500 self-consistency tests and for 1000 point source simulations. The shadows represent the standard deviations σ .

Distance effect

A study based on distances was carried out by using the new method of reconstruction. Like in section 4.4.1, the angles were fixed first at $(\theta = 90^\circ, \varphi = 180^\circ)$. For this angular configuration the source was placed at distances from 20 to 80 m and for each of these distances 1584 POCAM pulses were simulated with 10^9 photons each. The reconstructed angles in dependence of the distance are shown in Figure 4.31 and their standard deviations in Figure 4.32. The mean opening angles are depicted in Figure 4.33.

No relevant differences in the reconstruction between the two methods used are obtained for this study at $\theta = 90^\circ, \varphi = 180^\circ$ as a function of the distance. As in the previous method, although the mean opening angle and the standard deviations increase as the distance increases, if the mDOM is flashed a large number of times good mean values for the angular position of the source are obtained.

Table 4.7: Mean opening angle δ , $\theta_{\text{Likelihood}}$ and $\varphi_{\text{Likelihood}}$ values for 1584 point source simulation of 10^9 photons placed at $(\theta, \varphi) = (90^\circ, 180^\circ)$ for different distances.

Distance (m)	$\theta_{\text{Likelihood}}(^{\circ})$	$\varphi_{\text{Likelihood}}(^{\circ})$	Opening angle (δ ($^{\circ}$))
20	89.911 ± 0.014	180.458 ± 0.019	0.937 ± 0.011
25	89.823 ± 0.017	180.528 ± 0.025	1.152 ± 0.017
30	89.791 ± 0.021	180.59 ± 0.03	1.442 ± 0.022
35	89.720 ± 0.027	180.79 ± 0.04	1.802 ± 0.026
40	89.62 ± 0.03	180.99 ± 0.05	2.26 ± 0.03
45	89.65 ± 0.04	181.05 ± 0.06	2.74 ± 0.04
50	89.65 ± 0.05	181.25 ± 0.07	3.14 ± 0.04
55	89.55 ± 0.06	181.20 ± 0.07	3.61 ± 0.05
60	89.62 ± 0.08	181.46 ± 0.08	4.09 ± 0.05
65	89.73 ± 0.08	181.30 ± 0.08	4.40 ± 0.06
70	89.75 ± 0.10	181.28 ± 0.09	5.00 ± 0.07
75	89.61 ± 0.12	181.10 ± 0.10	5.51 ± 0.08
80	89.66 ± 0.14	181.38 ± 0.11	6.24 ± 0.09

A second study based on distances was carried out again placing the source at

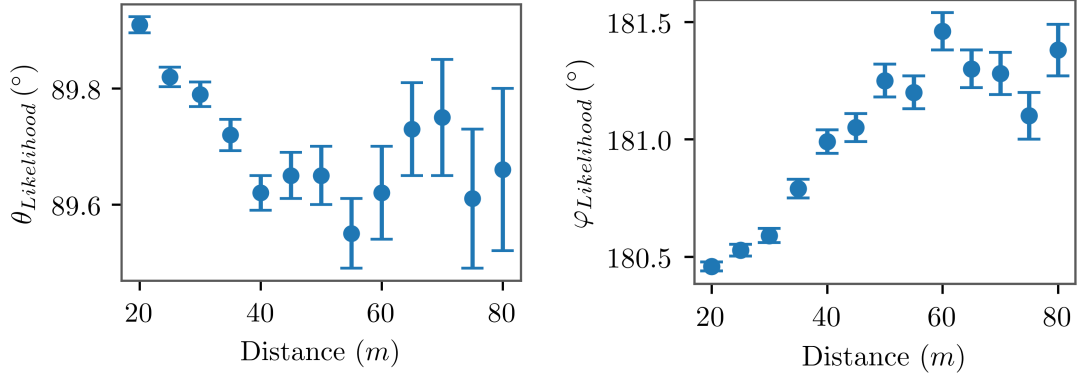


Figure 4.31: Mean $\theta_{\text{Likelihood}}$ (left) and $\varphi_{\text{Likelihood}}$ (right) for 1584 point source simulations placed at $(\theta, \varphi) = (90^\circ, 180^\circ)$ for different distances.

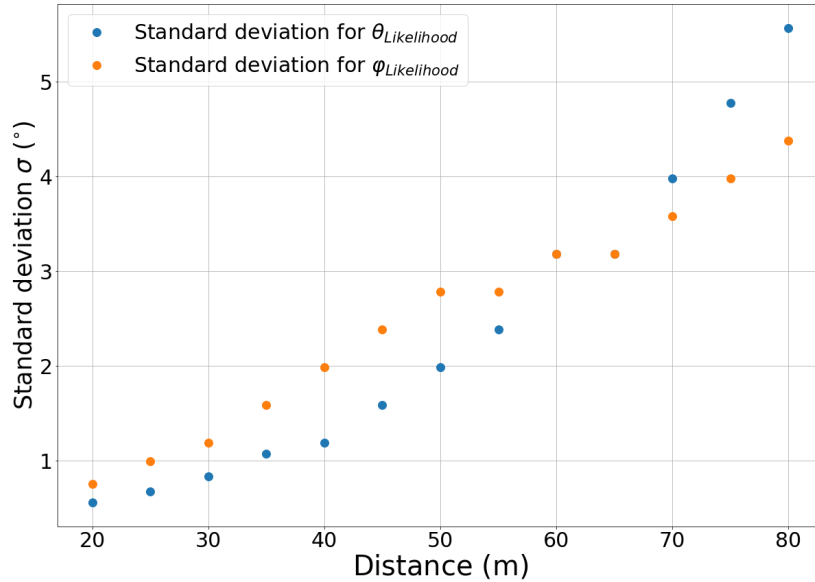


Figure 4.32: Standard deviation values for $\theta_{\text{Likelihood}}$ and $\varphi_{\text{Likelihood}}$ for 1584 point source simulations placed at $(\theta, \varphi) = (90^\circ, 180^\circ)$ at different distances.

$(\theta = 30^\circ, \varphi = 180^\circ)$. For this angular configuration, distances 10, 20, 50 and 100 m were taken. For each of these distances 1000 POCAM pulses were simulated with 10^9 photons each. The reconstructed angles in dependence of the distance are shown in Figure 4.34 and their standard deviations in 4.35. The mean opening angles are depicted in Figure 4.36. For the study in $\theta = 30^\circ$ as a function of the distance accurate mean values are obtained for the angular position of the

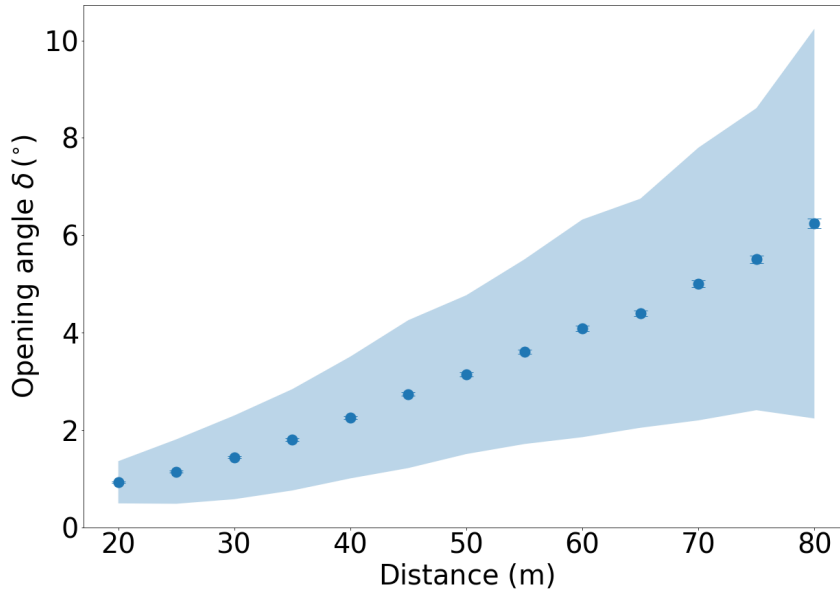


Figure 4.33: Mean opening angles between the true and reconstructed position of the point source for different distances. Source position at $(\theta, \varphi) = (90^\circ, 180^\circ)$. The shadow represents the standard deviation σ

source if the mDOM is flashed a large number of times. With respect to the reconstruction method previously used in which for $\theta = 30^\circ$ and POCAM pulses of $\sim 10^{12}$ photons, the values of the the opening angle mean values of the angular direction in θ were imprecise independent of the simulated (Table 4.4). With Likelihood method the standard deviations and the mean opening angle increase as the distance increases as in $\theta = 90^\circ$ case. But if the mDOM is flashed a large number of times good mean values of θ and φ are obtained in the reconstruction of the point source which means a good orientation calibration of the mDOM.

Table 4.8: θ and φ mean values for the Gaussian fit and opening angle δ mean value for 1000 point source simulations placed at $(\theta, \varphi) = (30^\circ, 180^\circ)$ for different distances.

Distance (m)	$\theta_{\text{Likelihood}}(^{\circ})$	$\varphi_{\text{Likelihood}}(^{\circ})$	Opening angle (δ ($^{\circ}$))
10	30.398 ± 0.019	180.14 ± 0.03	0.893 ± 0.015
20	29.874 ± 0.018	180.09 ± 0.05	1.124 ± 0.012
50	29.59 ± 0.07	179.90 ± 0.10	2.65 ± 0.05
100	30.92 ± 0.18	179.97 ± 0.29	8.02 ± 0.11

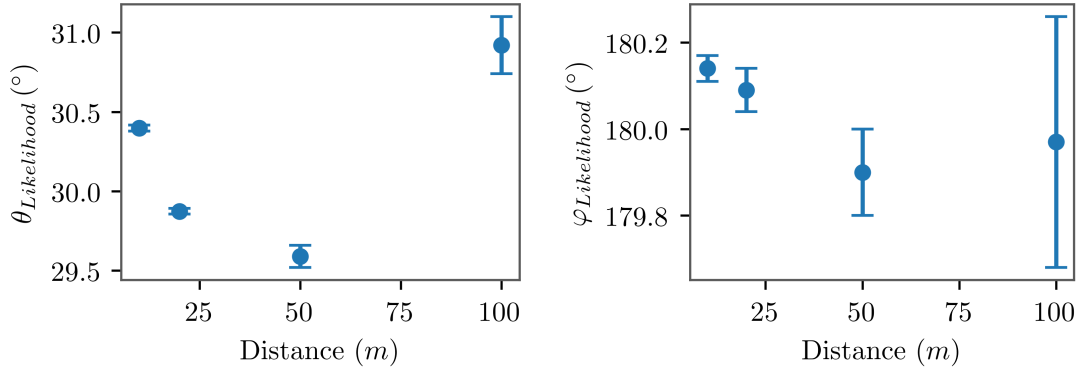


Figure 4.34: Mean θ_{Like} (left) and φ_{Like} (right) for 1000 point source simulations placed at $(\theta, \varphi) = (30^\circ, 180^\circ)$ for different distances.

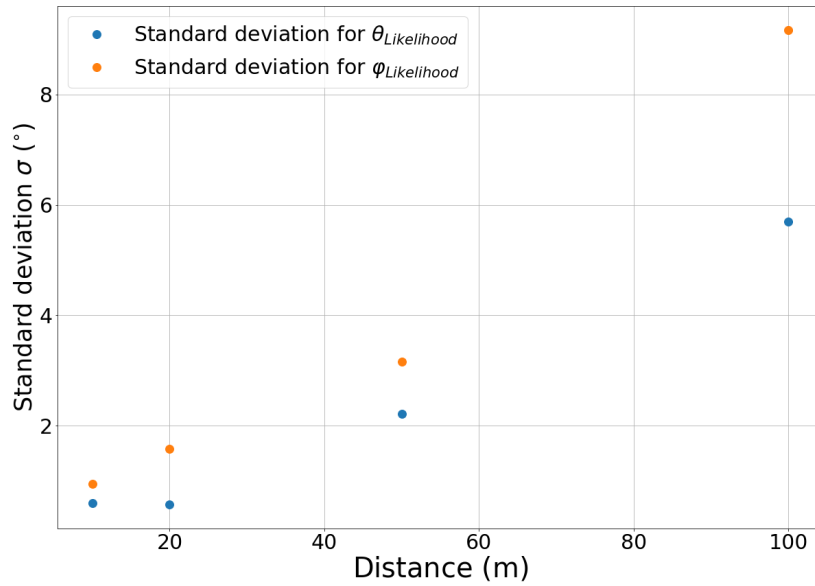


Figure 4.35: Standard deviation values for θ_{Like} and φ_{Like} for 1000 point source simulations placed at $(\theta, \varphi) = (30^\circ, 180^\circ)$ at different distances.

Depth effect

A study varying the depth of the mDOM in the simulation is performed here. As already said, the optical properties are not constant in the South Pole ice. This variation in the optical parameters of the ice causes the photons to have trajectories that may be deviated or absorbed due to the scatter or the absorption of the photon with greater or smaller probability depending on the depth. It is to be expected that better orientation reconstructions are performed at large

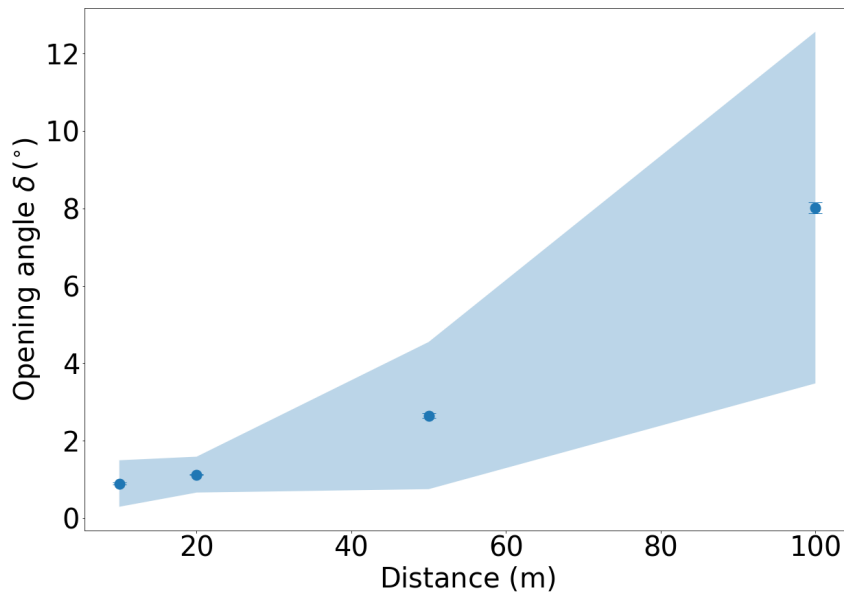


Figure 4.36: Mean opening angles between the true and reconstructed position of the point source for different distances. Source position at $(\theta, \varphi) = (30^\circ, 180^\circ)$.

scattering and absorption lengths, since more photons arrive to the mDOM. So far, the optical properties corresponding to a depth of 2278.2 m have always been simulated. This depth corresponds to the cleanest part of Antarctic ice ([30] and [24]).

Different depths were selected with the corresponding values of the optical parameters as shown in table 4.9. Two studies with all these depths have been carried out for distances 20 and 50 m.

It is observed that for the depths 1388.4 m, 1598.5 m and 1998.4 m the angular reconstruction is worse since this depths have smaller values for the absorption and scattering length, which means that photons are absorbed and scattered more often. For depths where scattering and absorption are most frequent, the module should be flashed a greater number of times in order to calibrate it.

Table 4.9: Optical properties (absorption length and scattering length) for different depths in the South Pole ice [30].

Depth (m)	Absorption length (m)	Scattering length (m)
1398.4	45.1	13.2
1498.4	135.6	39.7
1598.5	72.7	21.6
1698.5	113.9	30.6
1798.5	113.4	32.3
1898.5	143.6	38.4
1998.4	36.2	10.6
2098.5	173.1	54.3
2198.2	94.0	28.9
2298.0	223.9	75.6
2397.9	203.5	56.9

Table 4.10: Mean opening angles δ , $\theta_{\text{Likelihood}}$ and $\varphi_{\text{Likelihood}}$ for several point source simulation of 10^9 photons placed at $(\theta, \varphi) = (90^\circ, 180^\circ)$ and a distance of 20 m for different depths.

Depth (m)	Simulations	$\theta_{\text{Likelihood}}$ ($^\circ$)	$\varphi_{\text{Likelihood}}$ ($^\circ$)	Opening angle (δ) ($^\circ$)
1398.4	7	89.75 ± 0.25	182.0 ± 0.7	2.5 ± 0.4
1498.4	22	89.8 ± 0.5	180.6 ± 0.1	1.3 ± 0.4
1598.5	10	89.63 ± 0.14	182.0 ± 0.5	2.2 ± 0.4
1698.5	14	89.95 ± 0.04	180.73 ± 0.11	0.83 ± 0.05
1798.5	16	89.95 ± 0.03	180.85 ± 0.20	0.93 ± 0.18
1898.5	18	89.88 ± 0.25	180.81 ± 0.16	1.07 ± 0.25
1998.4	6	89.1 ± 0.4	183.1 ± 0.9	3.6 ± 0.6
2098.5	25	90.30 ± 0.17	180.16 ± 0.16	1.00 ± 0.13
2198.2	13	89.992 ± 0.008	180.88 ± 0.12	0.92 ± 0.10
2298.0	36	90.18 ± 0.09	181.05 ± 0.12	1.26 ± 0.09
2397.9	27	90.35 ± 0.17	180.72 ± 0.15	1.20 ± 0.15

New geometry effect

During the realization of the present work, the planned geometry for the mDOM was modified. This modification was carried out so that the cables holding the

Table 4.11: Mean opening angles δ , $\theta_{\text{Likelihood}}$ and $\varphi_{\text{Likelihood}}$ for 10 point source simulation of 10^9 photons placed at $(\theta, \varphi) = (90^\circ, 180^\circ)$ and a distance of 50 m for different depths.

Depth (m)	Simulations	$\theta_{\text{Likelihood}}$ ($^\circ$)	$\varphi_{\text{Likelihood}}$ ($^\circ$)	Opening angle (δ ($^\circ$))
1398.4	47	88.1 ± 0.4	183.89 ± 0.27	5.18 ± 0.21
1498.4	73	89.35 ± 0.14	181.68 ± 0.20	2.42 ± 0.16
1598.5	43	88.20 ± 0.44	184.2 ± 0.3	5.55 ± 0.21
1698.5	45	89.15 ± 0.25	182.65 ± 0.16	3.08 ± 0.23
1798.5	54	90.13 ± 0.18	182.91 ± 0.24	3.35 ± 0.20
1898.5	59	89.54 ± 0.11	182.27 ± 0.17	2.54 ± 0.15
1998.4	59	88.79 ± 0.26	184.41 ± 0.27	5.21 ± 0.18
2098.5	98	89.63 ± 0.04	181.88 ± 0.08	1.98 ± 0.08
2198.2	53	88.82 ± 0.29	182.61 ± 0.17	3.46 ± 0.21
2298.0	100	90.012 ± 0.022	181.19 ± 0.05	1.21 ± 0.05
2397.9	91	89.58 ± 0.04	181.79 ± 0.14	2.06 ± 0.11

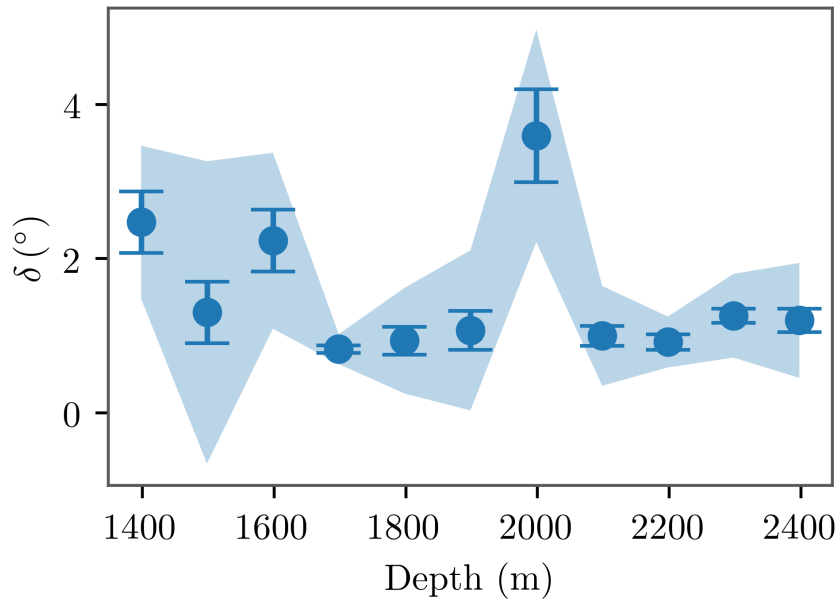


Figure 4.37: Mean opening angle δ values for several point source simulation of 10^9 photons placed at $(\theta, \varphi) = (90^\circ, 180^\circ)$ and a distance of 20 m for different depths.

module do not partially cover the surface of any PMT. The new geometry of the mDOM is shown in the Figure 4.39, where the northern and southern hemispheres

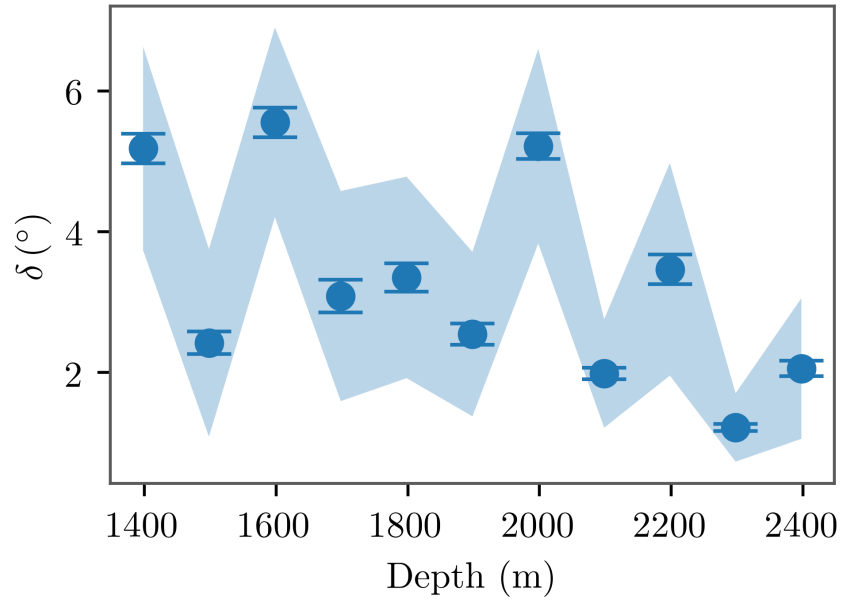


Figure 4.38: Mean opening angle δ values for several point source simulation of 10^9 photons placed at $(\theta, \varphi) = (90^\circ, 180^\circ)$ and a distance of 50 m for different depths.

are now symmetric. Since the scans were done with asymmetric hemispheres, new plane wavefront scans using HEALPix with the new mDOM geometry were simulated.

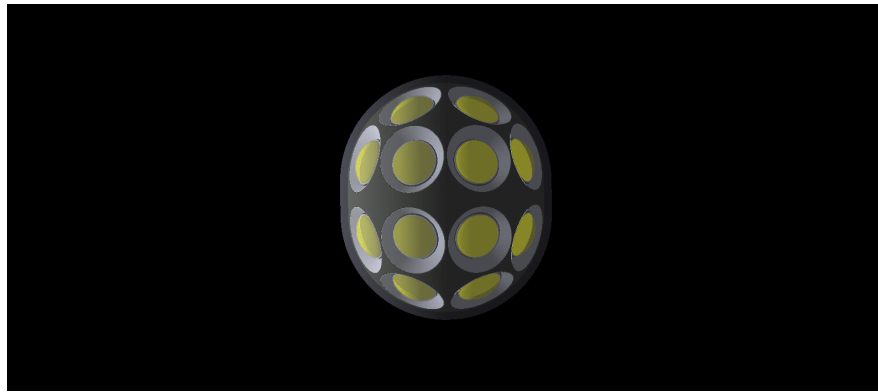


Figure 4.39: Simulated new mDOM geometry with symmetric northern and southern hemispheres.

The acceptance map is calculated again and it is shown in Figure 4.40. For this new geometry the inhomogeneity of the angular acceptance is $I = 15.5 \pm 0.2\%$ and thus practically the same between the two mDOM geometry.

The study for this new geometry of the mDOM was done only for an octant of the

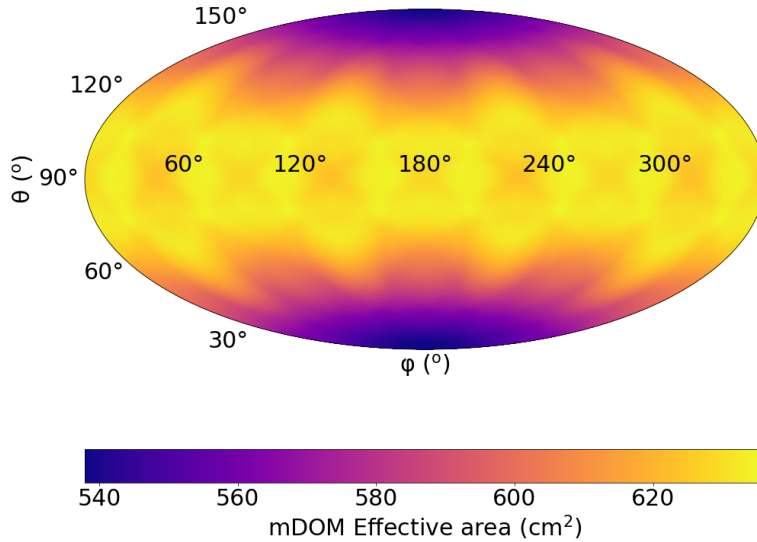


Figure 4.40: Acceptance map of the symmetric mDOM without QE shown as the angular effective area. It shows that the angular acceptance is near homogeneously distributed along the 4π . Incident light wavelength of 470 nm. 10^7 photons were simulated.

mDOM since due to its symmetry the results are completely reproducible for the rest of the octants making the convenient rotations. Point sources simulations of 10^9 photons placed at 20 m were performed again for different angular directions in an octant.

For this distance in table 4.12 one observes similar results to those obtained with the old mDOM geometry in table 4.6. Therefore, the uncertainty in the position of the source, or in other words, the uncertainty in the orientation of the mDOM does not show large differences between the two geometries of the mDOM.

The mean values of θ and φ obtained in the reconstructions using Likelihood method are still accurate in this new mDOM geometry even though the statistic is lower (only 500 simulations per direction). There is also no difference between the values corresponding to the standard deviations of the calculated mean values

Table 4.12: Mean opening angles δ , $\theta_{\text{Likelihood}}$ and $\varphi_{\text{Likelihood}}$ for different angular positions of the source. 500 simulations were run for each angular position.

Angular position of the source	$\theta_{\text{Likelihood}}$	$\varphi_{\text{Likelihood}}$	Opening angle (δ (°))
$(\theta, \varphi) = (90^\circ, 180^\circ)$	89.80 ± 0.10	180.00 ± 0.07	4.04 ± 0.03
$(\theta, \varphi) = (90^\circ, 210^\circ)$	89.95 ± 0.03	209.97 ± 0.03	0.751 ± 0.023
$(\theta, \varphi) = (90^\circ, 240^\circ)$	90.13 ± 0.03	240.07 ± 0.03	0.890 ± 0.018
$(\theta, \varphi) = (90^\circ, 270^\circ)$	90.11 ± 0.17	269.97 ± 0.06	3.98 ± 0.04
$(\theta, \varphi) = (120^\circ, 180^\circ)$	120.309 ± 0.027	179.90 ± 0.03	0.856 ± 0.016
$(\theta, \varphi) = (120^\circ, 210^\circ)$	120.91 ± 0.05	210.27 ± 0.03	1.38 ± 0.03
$(\theta, \varphi) = (120^\circ, 240^\circ)$	120.79 ± 0.04	239.54 ± 0.04	1.23 ± 0.03
$(\theta, \varphi) = (135^\circ, 180^\circ)$	134.95 ± 0.03	180.23 ± 0.04	0.899 ± 0.021
$(\theta, \varphi) = (135^\circ, 210^\circ)$	135.31 ± 0.03	210.32 ± 0.05	0.925 ± 0.024
$(\theta, \varphi) = (135^\circ, 240^\circ)$	135.23 ± 0.03	239.53 ± 0.05	0.947 ± 0.027
$(\theta, \varphi) = (150^\circ, 180^\circ)$	150.06 ± 0.03	180.15 ± 0.05	0.815 ± 0.021
$(\theta, \varphi) = (150^\circ, 210^\circ)$	150.82 ± 0.04	209.66 ± 0.12	1.64 ± 0.03
$(\theta, \varphi) = (150^\circ, 240^\circ)$	150.45 ± 0.03	240.41 ± 0.10	1.311 ± 0.027
$(\theta, \varphi) = (180^\circ, 180^\circ)$	174.466 ± 0.025	176 ± 5	5.53 ± 0.025

when compared with the old geometry. It indicates that the calibration in the mDOM orientation does not show large differences between the two different geometries.

5 Summary and outlook

This work presents a study on the calibration techniques in the orientation of the new modules that will be implemented in the next IceCube upgrade. For this, simulations have been carried out and an attempt has been made to reconstruct the direction of the incident light coming from an isotropic light point source by means of different techniques. The source simulates one of the new calibration devices that will be implemented in IceCube, the POCAM.

It was observed that the first technique used, which was developed in the thesis [36], provided precise reconstructions for a normal incidence of light on the mDOM, when it impacts on its equator and regions close to it. The reconstruction was still accurate despite increasing the distance between the light source and the mDOM. However, the reconstruction failed when the light hit on the areas farthest from the equator and close to the mDOM poles due the reconstruction technique, which did not correctly search for the biggest similarity between the scans and the point source simulations.

Therefore the method of reconstruction was changed to one more precise method, the maximum likelihood estimation, and drastically increasing both the number of simulations of scans performed on the mDOM and the directions of incidence of these scans, making their distribution homogeneous on the surface of a sphere.

It was observed that the precision in the angular reconstruction of the source was now practically constant for different directions of incidence of the light on the module. Hereby the problems shown by the first reconstruction method were solved.

A study with respect to the distances of the point source to the mDOM was carried out for the same depth (2278.2 m). As it was expected, the uncertainty in the position of the light source increases the further the point source is located from the module, since photons, since photons on their way to the mDOM are more likely to suffer absorption or scattering. But even though the uncertainty is increasing, good average values of $\theta_{Likelihood}$ and $\varphi_{Likelihood}$ are still obtained when carrying out numerous simulations with the same characteristics. These values of

$\theta_{Likelihood}$ and $\varphi_{Likelihood}$ are those calculated with the new reconstruction method, the Maximum likelihood estimation, and they correspond to the most probable position of the source.

Finally, a study with respect to the effects of the different optical properties of the ice layers on the reconstruction was performed. For different depths of the ice, the reconstruction is more precise when the absorption and scattering length values are larger, as expected, since the photons can travel larger distances before suffering any interaction with the ice.

The mDOM configuration changed during the realization of this master thesis so a brief study was made on the capacity of reconstruction of the light source position using this new mDOM configuration. The only difference between the two configurations is that in one of them the northern hemisphere is slightly rotated with respect to the other. It was observed that there are no significant differences when calibrating the orientation of a module or another. For both, precise values of the direction of incidence point source light are obtained and the uncertainty is similar.

In a real measurement there will be the quantum efficiency of the PMTs ($\sim 20 - 30\%$). Thus to have similar results in the number of hits to those made in this work, the mDOM should be flashed between 4 and 5 times more before reconstruction. This is not a problem since the POCAM can be flashed as many times as needed once it is placed in the ice, and the statistics can be simply summed up.

This work has therefore obtained that, using the techniques developed here, the POCAM will be able to calibrate orientation of the mDOM with an accuracy of about $\sim 1^\circ$ when flashing 10^{12} photons from 20 m .

Possible improvements that can be carried out in the future could be to have a more realistic situation, where in the same simulation the different ice layers and their optical properties are introduced. So, one could make a study based on the incidence angles of the point source while taking into account the depth where the source is. Up to now in our study the point source and the module have always been considered at the same level of depth and thus the optical parameters of the ice are constant within each simulation.

It could also be a good improvement to increase the statistics of the scans made on the detector by simulating a greater number of photons for each angular direction. Also increasing the number of homogeneous points on the spherical surface to have a greater number of scans on the mDOM would allow us to have a greater precision in the reconstruction using Maximum Likelihood Estimation. Last but not least, a detailed simulation of the POCAM, where this is not just approximated by a point source, should be performed in order to claim the angular sensitivity in a real case. In this simulation, one should also include the time distribution of the photons from the flash and study its possible effect on the angular reconstruction.

6 Bibliography

- [1] “Standard model wikipedia page.” https://en.wikipedia.org/wiki/Standard_Model, accessed: 2018.
- [2] M. G. Aartsen *et al.* (IceCube), *Science* **342**, 1242856 (2013), arXiv:1311.5238 [astro-ph.HE] .
- [3] C. E. Rolfs, W. S. Rodney, and W. A. Fowler, *Cauldrons in the cosmos : nuclear astrophysics*, Theoretical astrophysics (University of Chicago Press, Chicago u.a., 1988) pp. XVIII, 561 S.
- [4] I. V. Krivosheina, *Int. J. Mod. Phys.* **D13**, 2085 (2004).
- [5] G. Bellini *et al.* (Borexino), *Phys. Lett.* **B722**, 295 (2013), arXiv:1303.2571 [hep-ex] .
- [6] S. Betts *et al.*, in *Proceedings, 2013 Community Summer Study on the Future of U.S. Particle Physics: Snowmass on the Mississippi (CSS2013): Minneapolis, MN, USA, July 29-August 6, 2013* (2013) arXiv:1307.4738 [astro-ph.IM] .
- [7] C. Spiering, *Eur. Phys. J.* **H37**, 515 (2012), arXiv:1207.4952 [astro-ph.IM] .
- [8] J. K. Becker, *Phys. Rep.* **458**, 173 (2008), arXiv:0710.1557 .
- [9] U. F. Katz and C. Spiering, *Prog. Part. Nucl. Phys.* **67**, 651 (2012), arXiv:1111.0507 [astro-ph.HE] .
- [10] T. K. Gaisser, R. Engel, and E. Resconi, “Frontmatter,” in *Cosmic Rays and Particle Physics* (Cambridge University Press, 2016) pp. i–iv, 2nd ed.
- [11] A. Aab *et al.* (Pierre Auger), *Science* **357**, 1266 (2017), arXiv:1709.07321 [astro-ph.HE] .
- [12] A. Aab *et al.* (Pierre Auger), *Astrophys. J.* **868**, 4 (2018), arXiv:1808.03579 [astro-ph.HE] .
- [13] M. Ahlers, (2018), arXiv:1811.07633 [astro-ph.HE] .

- [14] A. Albert *et al.* (ANTARES, IceCube, LIGO, Virgo), (2018), arXiv:1810.10693 [astro-ph.HE] .
- [15] A. Albert *et al.* (ANTARES), *Astrophys. J.* **863**, L30 (2018), arXiv:1807.04309 [astro-ph.HE] .
- [16] A. D. Avrorin *et al.* (Baikal-GVD), (2018), arXiv:1810.10966 [astro-ph.HE] .
- [17] D. van Eijk, (2018), arXiv:1812.01036 [hep-ex] .
- [18] U. F. Katz (KM3NeT), *Proceedings, Vulcano Workshop 2010 : Frontier Objects in Astrophysics and Particle Physics: Vulcano, Italy, May 24-29, 2010*, Italian Phys. Soc. Proc. **103**, 563 (2011).
- [19] A. Albert *et al.* (ANTARES), (2017), arXiv:1711.01251 [astro-ph.HE] .
- [20] I. M. Frank and I. E. Tamm, *Compt. Rend. Acad. Sci. URSS* **14**, 109 (1937), [Usp. Fiz. Nauk93,no.2,388(1967)].
- [21] G. F. Knoll, *Radiation detection and measurement; 4th ed.* (Wiley, New York, NY, 2010).
- [22] M. Unland, *Studies on dark rates induced by radioactive decays of the multi-PMT digital optical module for future IceCube extensions*, https://www.uni-muenster.de/imperia/md/content/physik_kp/agkappes/abschlussarbeiten/masterarbeiten/1712-ma_munland.pdf, Master Thesis (2017).
- [23] F. Halzen and S. R. Klein, *Rev. Sci. Instrum.* **81**, 081101 (2010), arXiv:1007.1247 [astro-ph.HE] .
- [24] M. G. Aartsen *et al.* (IceCube), *Nucl. Instrum. Meth.* **A711**, 73 (2013), arXiv:1301.5361 [astro-ph.IM] .
- [25] M. G. Aartsen *et al.* (IceCube), *JINST* **12**, P03012 (2017), arXiv:1612.05093 [astro-ph.IM] .
- [26] R. Abbasi *et al.* (IceCube), *Nucl. Instrum. Meth.* **A601**, 294 (2009), arXiv:0810.4930 [physics.ins-det] .
- [27] “Icecube page.” <https://icecube.wisc.edu/gallery>, accessed: 2018.

- [28] J. van Santen (IceCube Gen2), *The Fluorescence detector Array of Single-pixel Telescopes: Contributions to the 35th International Cosmic Ray Conference (ICRC 2017)*, PoS **ICRC2017**, 991 (2018).
- [29] “Icecube neutrino observatory page.” <https://icecube.wisc.edu/news/view/605>, accessed: 2018.
- [30] M. Ackermann *et al.*, *J. Geophys. Res. Atmos.* **111**, D13203 (2006).
- [31] D. Chirkin (ICECUBE), *Proceedings, 33rd International Cosmic Ray Conference (ICRC2013): Rio de Janeiro, Brazil, July 2-9, 2013*, , 0580.
- [32] M. G. Aartsen and Ackermann (IceCube Collaboration), *Phys. Rev. D* **91**, 072004 (2015).
- [33] M. Rongen (IceCube), *Proceedings, 7th Very Large Volume Neutrino Telescope Workshop (VLVnT 2015): Rome, Italy, September 14-16, 2015*, EPJ Web Conf. **116**, 06011 (2016).
- [34] M. Jurkovič, K. Abraham, K. Holzappel, K. Krings, E. Resconi, and J. Veenkamp (IceCube Gen2), *Proceedings, 7th Very Large Volume Neutrino Telescope Workshop (VLVnT 2015): Rome, Italy, September 14-16, 2015*, EPJ Web Conf. **116**, 06001 (2016).
- [35] E. Resconi, K. Krings, and K. K. M. Rongen (IceCube Gen2), *The Fluorescence detector Array of Single-pixel Telescopes: Contributions to the 35th International Cosmic Ray Conference (ICRC 2017)*, PoS **ICRC2017**, 934 (2018).
- [36] L. Classen, *Prototyping a multi-PMT optical module for the IceCube-Gen2 neutrino telescope*, https://www.uni-muenster.de/imperia/md/content/physik_kp/agkappes/abschlussarbeiten/doktorarbeiten/1702-phd_1classen.pdf, PhD thesis (2017).
- [37] B. Herold, *Simulation and measurement of optical background in the deep sea using a multi-PMT optical module*, PhD thesis, Friedrich-Alexander-Universität Erlangen- Nürnberg (2017).
- [38] “Geant4 website,” <https://geant4.web.cern.ch/geant4/>, accessed: 2018.
- [39] S. Agostinelli *et al.* (GEANT4), *Nucl. Instrum. Meth.* **A506**, 250 (2003).

[40] R. J. Barlow, *Statistics: A Guide to the Use of Statistical Methods in the Physical Sciences (Manchester Physics Series)* (Wiley, 1989).

[41] “Healpix page.” <https://healpix.sourceforge.io/>, accessed: 2018.

List of Figures

- 2.1 A depiction of the elementary particles in the standard model: The 12 fundamental fermions (purple and green) and 5 fundamental bosons (red). Fermions are constituted by quarks (purple) and leptons (green). Figure taken from [1] 4
- 2.2 Neutrino fluxes detected on Earth from different sources. The region from tens of GeV to about 100 PeV, which feature much smaller fluxes than neutrinos of smaller energies, is addressed by Cherenkov light detectors. The highest energies are only accessible with huge volume detectors like IceCube. Figure taken from [7] 6
- 2.3 Cherenkov radiation cone along the trajectory of a fast moving charged particle with speed u that moves faster than light in that medium. θ is the angle between the direction of movement of the charged particle and the Cherenkov photons. 8
- 2.4 Schematic of a photomultiplier tube and its main constituents. The green sinusoidal line represents a photon that emits a photoelectron (blue line) at the photocathode realising secondary electrons from the dynodes. The total charge is collected at the anode. Figure taken from [22] 10
- 3.1 **Left:** Image of the IceCube Observatory at the South Pole with all their components: the high-energy array, the low-energy extension DeepCore and IceTop on the surface. **Right:** Image of The IceCube DOM. It consists of a glass pressure sphere with a 10 inch PMT facing down in the lower half and readout electronics. Figures taken from [27]. 12

3.2	Light deposition signatures of a shower (left) and a track (right). Modules are drawn as dots, the color gives information about the arrival time of photons, going from red (early) to blue (later) and the size of the dots about the amount of detected light. Figure taken from [27]	13
3.3	Expected double bang event signature from a high energetic τ neutrino. This event have been simulated even though there are already some double bang candidates. Figure taken from [27]	13
3.4	A possible IceCube-Gen2 configuration. IceCube, in red, and the infill subdetector DeepCore, in green, show the current configuration. The blue volume shows the full instrumented next-generation detector. Figure taken from [27]	14
3.5	The modules of the IceCube Upgrade will be deployed with vertical and horizontal spacings three times smaller than DeepCore. Figure taken from [27].	15
3.6	Deep ice optical properties. Absorption length (left) and scattering length (right) of light in the South Pole ice as a function of depth, from 1100 m to 2300 m and wavelength, from 300 to 600 nm. Figure taken from [30].	19
3.7	Left: Rendered image of the mDOM with 24 PMTs inside the pressure vessel. Right: Exploded view of the mDOM, with its different components. Courtesy of the IceCube Collaboration. . .	20
3.8	POCAM design: It is composed of four sub-systems: the pressure housing, the digital and the analog circuit boards, and the light diffuser elements.	23
4.1	Left: Scan simulation for a certain angular position made on the mDOM in which photons are simulated from the normal direction to a plane disc. Right: POCAM simulated as an isotropic point source.	26

4.2	mDOM illumination from $(\theta = 45^\circ, \varphi = 0^\circ)$ (left) and $(\theta = 90^\circ, \varphi = 0^\circ)$ (right). Figure taken from [36].	27
4.3	Angular effective area for two PMTs of the module without quantum efficiency for an incident plane wavefront of 470 nm. 10^7 photons were simulated per angle pair.	28
4.4	Acceptance map of the mDOM shown as the angular effective area with a near homogeneous 4π angular acceptance. The incident light has a wavelength of 390 nm which corresponds to the maximum quantum efficiency of the PMTs. 10^6 photons were simulated per angle pair. Result from [36]	29
4.5	Acceptance map of the mDOM without consideration of quantum efficiency shown as the angular effective area with a near homogeneous 4π angular acceptance. The incident light has a wavelength of 470 nm. 10^7 photons were simulated per angle pair.	30
4.6	Left: $P(\theta, \varphi)$ distribution map of the source position. Simulated position of the source $(\theta = 90^\circ, \varphi = 180^\circ)$. Right: Gaussian fit around the maximum of the probability map.	32
4.7	Histograms of θ (left) and φ (right) fitted gaussians values for 1200 simulations of point source when the source is placed at $(\theta = 90^\circ, \varphi = 180^\circ)$ 20 meters away from the mDOM.	33
4.8	Opening angle histogram of 1200 point source simulations.	33
4.9	Mean reconstructed θ_{Gauss} (left) and φ_{Gauss} (right) for 900 point source simulations for different distances.	35
4.10	Standard deviation values for θ_{Gauss} and φ_{Gauss} for 900 point source simulations placed at $(\theta, \varphi) = (90^\circ, 180^\circ)$ at different distances.	35
4.11	Mean opening angles values for 900 point source simulations placed at $(\theta, \varphi) = (90^\circ, 180^\circ)$ at different distances. The shadow represents the standard deviation σ of these results for each distance.	36

- 4.12 Probability map of the source position for a single point source simulation. The maximum of the probability map, the gaussian fit maximum and the real position of the source were marked. **Top:** Simulated position of the source ($\theta = 90^\circ, \varphi = 60^\circ$) (left), ($\theta = 90^\circ, \varphi = 240^\circ$) (right). **Bottom:** Simulated position of the source ($\theta = 90^\circ, \varphi = 120^\circ$) (left), ($\theta = 90^\circ, \varphi = 300^\circ$) (right). 37
- 4.13 Probability map of the source position for a single point source simulation. The maximum of the probability map, the gaussian fit maximum and the real position of the source were marked. **Top:** Simulated position of the source ($\theta = 30^\circ, \varphi = 180^\circ$) (left), ($\theta = 135^\circ, \varphi = 180^\circ$) (right). **Bottom:** Simulated position of the source ($\theta = 120^\circ, \varphi = 180^\circ$) (left), ($\theta = 150^\circ, \varphi = 180^\circ$) (right). 38
- 4.14 Deviation of the mean θ_{Gauss} values respect to the real position θ_{True} (left) and Deviation of the mean φ_{Gauss} values respect to the real position φ_{True} (right) of the source when varying coordinate φ . The shadow represents the standard deviation σ 39
- 4.15 Deviation of the mean θ_{Gauss} values respect to the real position θ_{True} (left) and Deviation of the mean φ_{Gauss} values respect to the real position φ_{True} (right) of the source when varying coordinate θ . The shadow represents the standard deviation σ 40
- 4.16 Mean opening angles values when the source is moved around φ axis (left) and θ axis (right). The shadow represents the standard deviation σ of these opening angles. The reconstruction is inaccurate when θ is varied. 40
- 4.17 **Left:** Cuts in the probability maps for $\theta = 90^\circ$ and different values of the source in φ . **Right:** Cuts in the probability map for $\varphi = 180^\circ$ and different values of the source in θ . It is noticeable how, varying θ , the probability maps are moved slightly towards $\theta = 90^\circ$ which corresponds to the equator of the mDOM. 41

4.18	Source location probabilities for a point source placed at $(\theta, \varphi) = (30^\circ, 180^\circ)$ for different distances between the source and the module. The distance does not affect the movement of the maximum of the probability towards the equator of the mDOM.	42
4.19	Probability map of the source position for different distances. Simulated position of the source ($\theta = 30^\circ, \varphi = 120^\circ$). The maximum of the probability map, the gaussian fit maximum and the real position of the source were marked. Top: Distance 10 m (left), distance 20 m (right). Bottom: Distance 50 m (left), distance 100 m (right).	43
4.20	Cumulative distribution function for the Likelihood method.	45
4.21	Cuts in the Likelihood maps where the maximum is not shifted. Left: $\theta = 90^\circ$ and different angular positions of the source for φ . Right: $\varphi = 180^\circ$ and different angular positions of the source for θ	46
4.22	Healpix distribution of points around the spherical coordinates θ and ϕ for different number of pixels. Figure taken from [41]	47
4.23	Likelihood map for a single point source simulations at 20 m and ($\theta = 90^\circ, \varphi = 180^\circ$). The σ region is bounded by the red line and the 2σ region by the black line.	49
4.24	Histogram of $\theta_{\text{Likelihood}}$ (left) and $\varphi_{\text{Likelihood}}$ (right) reconstructed values for 1000 point source simulations at 20 m and ($\theta = 90^\circ, \varphi = 180^\circ$).	49
4.25	Histogram of opening angles δ values for 1000 point source simulations at 20 m and ($\theta = 90^\circ, \varphi = 180^\circ$).	50
4.26	Deviation of the mean $\theta_{\text{Likelihood}}$ values respect to the real position θ_{True} (left) and Deviation of the mean φ_{Gauss} values respect to the real position φ_{True} (right) of the source when varying coordinate φ	51
4.27	Deviation of the mean $\theta_{\text{Likelihood}}$ values respect to the real position θ_{True} (left) and Deviation of the mean φ_{Gauss} values respect to the real position φ_{True} (right) of the source when varying coordinate θ	52

4.28	Mean opening angles values when the source is moved around φ axis (left) and θ axis (right). The shadow represents the standard deviation σ of these opening angles.	52
4.29	Standard deviations of reconstructed values when the source is moved around θ axis (left) and φ axis (right).	53
4.30	Mean opening angles for 500 self-consistency tests and for 1000 point source simulations. The shadows represent the standard deviations σ	53
4.31	Mean $\theta_{\text{Likelihood}}$ (left) and $\varphi_{\text{Likelihood}}$ (right) for 1584 point source simulations placed at $(\theta, \varphi) = (90^\circ, 180^\circ)$ for different distances. . .	55
4.32	Standard deviation values for $\theta_{\text{Likelihood}}$ and $\varphi_{\text{Likelihood}}$ for 1584 point source simulations placed at $(\theta, \varphi) = (90^\circ, 180^\circ)$ at different distances.	55
4.33	Mean opening angles between the true and reconstructed position of the point source for different distances. Source position at $(\theta, \varphi) = (90^\circ, 180^\circ)$. The shadow represents the standard deviation σ . .	56
4.34	Mean θ_{Like} (left) and φ_{Like} (right) for 1000 point source simulations placed at $(\theta, \varphi) = (30^\circ, 180^\circ)$ for different distances.	57
4.35	Standard deviation values for θ_{Like} and φ_{Like} for 1000 point source simulations placed at $(\theta, \varphi) = (30^\circ, 180^\circ)$ at different distances. . .	57
4.36	Mean opening angles between the true and reconstructed position of the point source for different distances. Source position at $(\theta, \varphi) = (30^\circ, 180^\circ)$	58
4.37	Mean opening angle δ values for several point source simulation of 10^9 photons placed at $(\theta, \varphi) = (90^\circ, 180^\circ)$ and a distance of 20 m for different depths.	60
4.38	Mean opening angle δ values for several point source simulation of 10^9 photons placed at $(\theta, \varphi) = (90^\circ, 180^\circ)$ and a distance of 50 m for different depths.	61

4.39 Simulated new mDOM geometry with symmetric northern and southern hemispheres.	61
4.40 Acceptance map of the symmetric mDOM without QE shown as the angular effective area. It shows that the angular acceptance is near homogeneously distributed along the 4π . Incident light wavelength of 470 nm. 10^7 photons were simulated.	62

List of Tables

4.1	Description of the different physical processes and their corresponding class in Geant4 for the particle of interest in the simulations, the photon.	26
4.2	Mean opening angle δ and average reconstructed angles $(\theta_{Gauss}, \varphi_{Gauss})$ for 900 point source simulations placed at $(\theta, \varphi) = (90^\circ, 180^\circ)$ for different distances.	34
4.3	Opening angle, θ_{Gauss} , φ_{Gauss} mean values for different angular positions of the source. 500 POCAM flashers were simulated for each angular position.	39
4.4	θ_{Gauss} and φ_{Gauss} values for the Gaussian fit and opening angle δ for point source simulations placed at $(\theta, \varphi) = (30^\circ, 180^\circ)$ at different distances.	41
4.5	Mean opening angle for 500 self-consistency tests for different incident angular directions of the plane wavefront. The uncertainty comes from a purely statistical effect when applying Poisson on the re-scaled hits in each PMT.	48
4.6	Mean opening angles δ , $\theta_{Likelihood}$ and $\varphi_{Likelihood}$ for different angular positions of the source. 1000 simulations were run for each angular position.	51
4.7	Mean opening angle δ , $\theta_{Likelihood}$ and $\varphi_{Likelihood}$ values for 1584 point source simulation of 10^9 photons placed at $(\theta, \varphi) = (90^\circ, 180^\circ)$ for different distances.	54
4.8	θ and φ mean values for the Gaussian fit and opening angle δ mean value for 1000 point source simulations placed at $(\theta, \varphi) = (30^\circ, 180^\circ)$ for different distances.	56
4.9	Optical properties (absorption length and scattering length) for different depths in the South Pole ice [30].	59

4.10	Mean opening angles δ , $\theta_{\text{Likelihood}}$ and $\varphi_{\text{Likelihood}}$ for several point source simulation of 10^9 photons placed at $(\theta, \varphi) = (90^\circ, 180^\circ)$ and a distance of 20 m for different depths.	59
4.11	Mean opening angles δ , $\theta_{\text{Likelihood}}$ and $\varphi_{\text{Likelihood}}$ for 10 point source simulation of 10^9 photons placed at $(\theta, \varphi) = (90^\circ, 180^\circ)$ and a distance of 50 m for different depths.	60
4.12	Mean opening angles δ , $\theta_{\text{Likelihood}}$ and $\varphi_{\text{Likelihood}}$ for different angular positions of the source. 500 simulations were run for each angular position.	63

Acknowledgments

First and foremost, I want to thank to my advisor in this thesis, Prof. Dr. Alexander Kappes, for giving me the opportunity to work in his group. I would like to thank his guidance, advice and infinite patient. I would also like to thank my second supervisor, Dr Javier García López, who has kindly offered me his support.

Thanks also to Lew Classen, Cristian Lozano and Martin Unland, who guided me from the very first moments. Thanks a lot for your help, guidance and support.

Por último, pero no por ello menos importante sino todo lo contrario, quiero dar las gracias a mi familia. En especial a mis padres, por su incansable apoyo y confianza durante la realización tanto de mi master como de todos mis estudios. Os quiero y os querré siempre.

Declaration of Academic Integrity

I hereby confirm that this thesis on "Simulation studies towards an orientation calibration technique for the multi-PMT digital optical module in future IceCube extensions" is solely my own work and that I have used no sources or aids other than the ones stated.

Juan Bautista Bernal Florindo

Münster, December 2018

I agree to have my thesis checked in order to rule out potential similarities with other works and to have my thesis stored in a database for this purpose.

Juan Bautista Bernal Florindo

Münster, December 2018